

METHODS IN BIOENGINEERING SERIES

Kaushal Rege
Igor L. Medintz

editors

METHODS IN BIOENGINEERING

NANOSCALE
BIOENGINEERING
AND NANOMEDICINE

Porous Silicon Particles for Multistage Delivery

Ennio Tasciotti,^{1*} Jonathan Martinez,¹ Ciro Chiappini,² Rohan Bhavane,¹ and Mauro Ferrari^{1,2,3,4}

¹The Division of Nanomedicine, Department of Biomedical Engineering, The University of Texas Health Science Center at Houston, Houston, TX 77030

²Department of Biomedical Engineering, The University of Texas, Austin, TX 77030

³Department of Experimental Therapeutics, The University of Texas MD Anderson Cancer Center, Houston, TX 77030

⁴Department of Bioengineering, Rice University, Houston, TX 77005

*Corresponding author: Ennio Tasciotti, Ph.D., Assistant Professor, Department of Nanomedicine and Biomedical Engineering, Division of Nanomedicine, Institute for Molecular Medicine, 1825 Pressler Street, Suite 537B, Houston, TX 77030; e-mail: Ennio.Tasciotti@uth.tmc.edu, Phone: (713) 500-2468, Fax: (713) 500-2462

Abstract

In this chapter, we present a novel multistage delivery system (MDS) to address the inherent complexity involved in drug delivery. The proposed system has the potential to revolutionize the delivery of therapeutics at target lesions by distributing the tasks of biobarrier avoidance, targeting, and therapeutic effect among different vector stages. The first-stage vector of this MDS system is a microfabricated nanoporous silicon particle with tailored chemo-physical and geometrical properties. The subsequent stages can be selected among a wide range of nano-sized carriers or therapeutics. Employing the MDS, investigators can concentrate on synthesizing novel and innovative therapies disregarding the issues of targeting and biobarrier avoidance that will be addressed by the first stage of the MDS.

Key terms

multistage
porous silicon
drug delivery
imaging
tunable porosity/pore size
nanovectors
biodegradable
biobarrier avoidance

13.1 Introduction

The detection of trace markers in clinical samples and the localization of carriers to diseased body sites are the ultimate goals for effective disease diagnosis/prevention, and treatment [1, 2]. The ability to obtain sensitive data in a noninvasive manner and to concentrate therapeutic compounds at the target sites are among the most crucial, breakthrough applications currently needed in the clinic. Over the last three to five decades, cancer treatment has relied upon surgical removal of the primary tumor, followed by the use of radiation, and then repeated cycles of the maximum-tolerated doses of a combination of cytotoxic chemotherapeutic agents. Unfortunately, the vast majority of malignancies have proven to be resistant to this type of chemotherapeutic intervention, partially due to the requisite dose limitations for preventing adverse effects on normal tissues. Conventional cancer chemotherapeutics gain access to the blood stream through intravenous administration and are required to penetrate the extravascular space in order to present the drug at an adequate concentration such to inflict lethal toxicity to the tumor lesion. Even the best injectable drug to date retains its specificity of action only through its molecular affinity for the ultimate therapeutic substrate while remaining completely indifferent to its own distribution within the body. Effective cancer therapy continues to present the drug delivery conundrum of right treatment, right cell, and right dose, with minimal collateral damage. Additionally, 40% of new anticancer compounds fail to enter clinical trials due to solubility or systemic toxicity issues. Despite advances in drug discovery, the transition to the clinical setting remains challenged by the inability to efficiently deliver the right compound to the best in vivo target. To address this issue, a plethora of different vectors have been proposed as the ideal candidates to the time-honored problem of optimizing the therapeutic index for treatment (i.e., to maximize efficacy, while reducing health-adverse side effects).

To provide effective drug delivery, the carriers must be capable of reaching and recognizing their target site. Nanomaterial characteristic size, close to that of cell components, allowed the development of tools capable of interfacing directly with the pillar constituents of life: nucleic acids, proteins, and biological molecules. Thanks to these unique features, nanotechnology and the nanotechnology toolset hold great promises in the field of drug delivery and have the potential to revolutionize this research area, enabling a paradigmatic shift from molecularly targeted therapeutics to cell or site directed therapeutics [3]. As a result, the drug diffuses without differentiation among all the body tissues, becoming activated at nonspecific sites and generating adverse side effects, thus lowering the therapeutic index [4]. Among the various classes of nanoparticles (NP) developed for drug delivery (dendrimers, liposomes, nanotubes, and so forth), very few are amenable for the optimizations (surface modification, targeting, surface stealthing, and particle size/shape) required to obtain an individualized delivery strategy and to improve their efficacy. In order to maintain their therapeutic level, the carriers must be able to efficiently negotiate the biobarriers from the point of entry to the target. Hemorheology [5], Reticulo-Endothelial System (RES) cells [6], thrombocytes and erythrocytes [7], attack by lytic enzymes [8], crossing of the endothelial wall [9] or blood brain barrier (BBB) [10], diffusion in the perivascular tissue against the interstitial and osmotic pressure [11, 12], and entry into the cell cytoplasm through the cell membrane [13] constitute only part of the many sequential biobarriers that stand between the carrier and its target site. These mechanisms, intended to oppose harmful entities, do not discriminate between potentially beneficial delivery vectors and harmful foreign bodies.

As a consequence, these barriers pose as insurmountable obstacles for any prototypical drug or nano-therapeutic to overcome [14]. Of the vast and diverse array of NPs developed in laboratories, only a handful have made their way to the clinic [15]. This shortcoming can be traced to the inability to develop a NP capable of sequentially negotiating all the biological barriers in an effective manner. As an example, surface functionalization with poly-ethyleneglycol (PEG) prevents particles from being rapidly scavenged by the RES [16], but also limits their ability to be recognized and internalized by the target cells. Recently, the concept of NP engineering has revolutionized the battle against the biological barriers. For example, appropriate engineering of NP size and shape allows them to reach tumor sites exploiting the enhanced permeability and retention (EPR) effect (passive targeting) [17]; localization at a lesion site can also be actively sought conjugating targeting molecules chosen from a vast array of antibodies, ligands, peptides, aptamers, or phages [18–24]. Fusion with the cell membrane can be facilitated by conjugation of the NPs with cell penetrating peptides [25], and release from lysosomes can be triggered by chemical sensors on the NPs [26]. A successful NP must then be endowed with multiple, and often conflicting, functions. In most, if not all cases, it is practically impossible to provide a single NP with all the necessary tools to achieve these goals [27, 28].

The current pharmaceutical and biotechnological paradigm for a successful therapeutic is to embody in it three critical functions: cytotoxic action, biological recognition, and avoidance of biological barriers. An elegant solution to this challenge is a new class of drug delivery vectors in which these essential tasks have been distributed among a larger number of components within a coordinated system. The components can be assembled *ex vivo* with the objective of addressing the biological barriers in a multiplexed, sequential, independent yet synergistic way. Our laboratory recently proposed a new class of nanotechnology delivery vectors and a new approach called the Multistage Delivery Systems (MDS) [29] (Figure 13.1). This new vision decouples the tasks required from therapeutics, assigning to the first-stage delivery vectors the role of biobarrier avoidance, first-order localization, and the conventional biorecognition modalities. The second-stage NPs, nested within the first stage, are endowed with the ability of penetrating into the lesion exploiting EPR or with the help of permeation enhancers and thus selectively directing their cytotoxic payload against target cells and tissues. The first-stage particle's engineered geometry assists in protecting the second-stage NPs while the system navigates the vasculature. Once the first-stage particles reach the final docking place on the vascular endothelium, adjacent to the target site, the second-stage NPs are released and diffuse in the perivascular tissue, where they can accomplish their final tasks. The nanoporous silicon particles (PSP) constitute the primary vector of the MDS. These first-stage PSPs are biodegradable and biocompatible [30], and their size, shape, porosity, and pore size can be finely tuned during the manufacturing processes [31–33]. The chemo-physical properties of these PSPs are tailored according to rational design guided by a strong mathematical toolset, in order to obtain the desired functionality. Mathematical modeling of the effects of the geometry on the vascular navigation behavior of micro and NPs provides optimal solutions for biodistribution, adhesion, and endocytosis [34]. The vast repertoire of chemical functionalizations achievable on silicon surfaces enables the PSPs to address and overcome some of the aforementioned biological barriers [35–37]. Finally, the release kinetics of the second-stage NPs can be linked

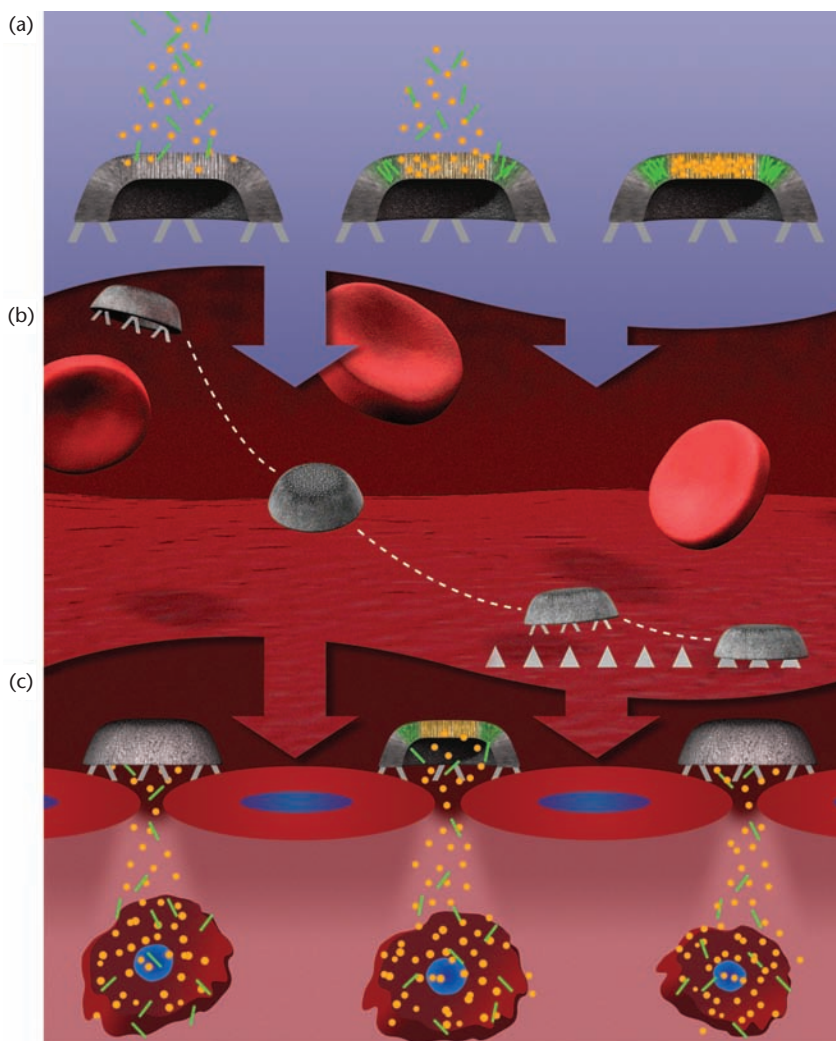


Figure 13.1 Schematic depicting the process of the multistage delivery system. (a) The MDS is first assembled by loading second-stage NPs into the pores of the PSPs. (b) After i.v. injection, these rationally designed PSPs travel through the blood stream and due to their size, shape, and surface modifications avoid RES uptake and finally migrate to the vessel wall where they can adhere to the target's endothelium (c) Once docked, the PSPs release their payload (second-stage NPs), which will penetrate through the natural fenestrations of the target's vasculature and eventually diffuse into the tissue, where they will be taken up and accomplish their final task. (Reproduced with permission from [29] courtesy of Nature Publishing Group.)

to the degradation rates of the first stage PSPs through the adjustment of porosity, pore size, and pore distribution on the silicon carrier [38].

Different approaches can be employed to capture, enclose, and carry the intended functional cargoes, and recently, alternative multifunctional systems for the delivery of biological agents have been proposed. These systems take advantage of bacterial strains [39, 40], T lymphocytes [41], and phages [42] to incorporate or target agents and nanoparticles to induce a cytotoxic effect on selected cell types.

Ferrite oxide particles have been enveloped in the cytoplasmic bacterial wall and modified with polyethylenimine (PEI), a proven effective gene carrier, to improve the

transfer of genetic material into target cells. The authors refer to this multifunctional system as bacterial magnetic particles-PEI (BMP-PEI) complexes [40].

The “microbots” (Figure 13.2) are a multistage delivery system that exploits live bacteria to mediate the delivery of bioactive agents into cells [39]. The choice of bacterial strains with particular physiological properties allowed for the development of distinct delivery applications. In this system the cargo is conjugated on the surface of the bacteria, rather than being loaded inside the cytoplasm. This type of conjugation avoids bacterial disruption in order to take advantage of the natural tropism of the bacteria to the host tissues. However, both these methods are limited in the type of nanoparticles that can be effectively delivered. The BMP-PEI system allows for the delivery of DNA and is limited by its lack of flexibility towards the delivery of other nano-agents. Microbots could not deliver more than an average of 22 200-nm particles per cell, while our silicon-based MDS method can deliver an average of 20 microparticles per cell, each loaded with thousands of NPs. Moreover, the microbots, when not immediately internalized by cells, expose the conjugated nanoparticles to the hostile environment within the vasculature, while the MDS protects the payload inside the nanopores. Lastly, the functionalization leading to the conjugation of nanoparticles prevents further decoration of the bacteria with targeting moieties, rendering it unfit for intravascular delivery and susceptible to nonspecific interaction with the biological barriers.

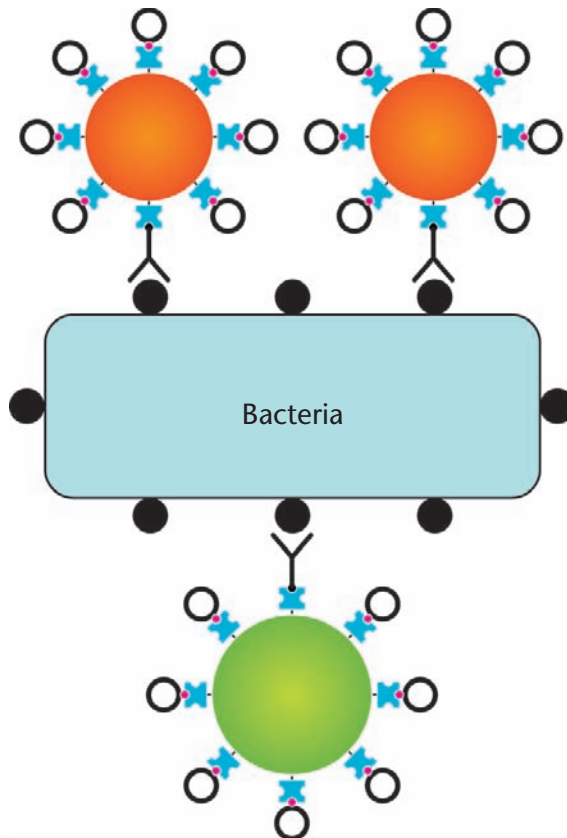


Figure 13.2 Schematic of a microbot. The nanoparticles, labeled with imaging moieties, are conjugated on the surface of the bacteria. (Adapted from [39].)

In another MDS, the transport of therapeutic agents is mediated by T lymphocytes [41]. In this system, lymphocytes would be isolated from the patient and then incubated or electroporated with desired nanoparticles. The cargo is efficiently protected from the biobarriers once reintroduced into the patient (Figure 13.3). This type of system allows for localized drug targeting and detection of metastases and could possibly be combined with existing immunotherapies. The method, however, is greatly limited by the inconsistent and scarcely controllable loading and release kinetics of the nanoparticles. In addition, the nanoparticles might have a detrimental effect on the targeting ability of the lymphocytes.

The last class of MDS is a network of bacteriophage and gold nanoparticles (Figure 13.4) [42]. The phages are engineered in such a way that each phage displays a peptide. This peptide can be selected among a huge combinatorial library in order to target a specific receptor expressed, for example, on the surface of an endothelial cells. These Au-phage complexes can be designed to specifically target cells for imaging or thermal ablation purposes. Nevertheless, this network of nanoparticles may still be vulnerable to biobarriers due to their overall size, and its best use would probably be as a payload or as a targeting moiety embedded or attached into a larger multifunctional system.

The success of any MDS relies on the ability to accurately engineer its components, decorate its surface, and govern the loading and release of the various stages. In this

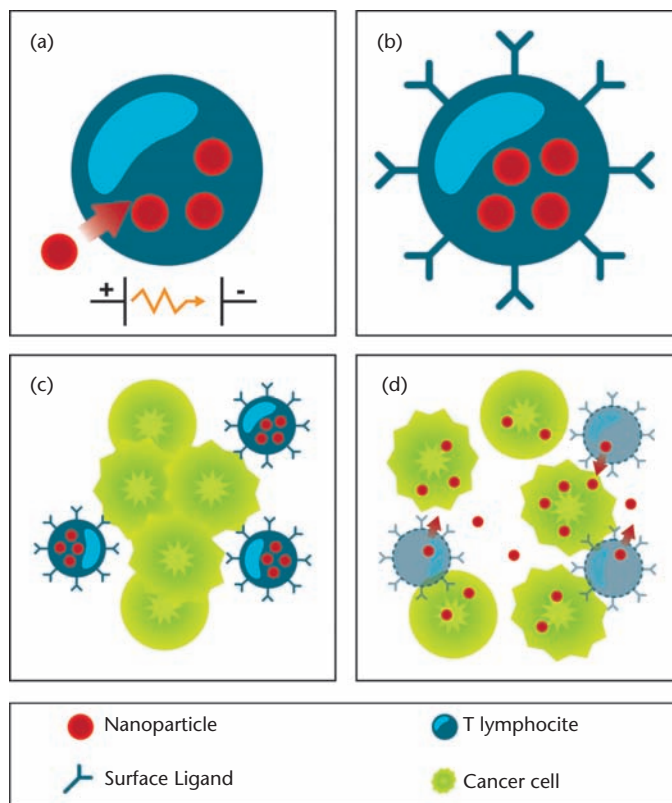


Figure 13.3 (a–d) Schematic of T-lymphocytic delivery of loaded nanoparticles to cancer cells.

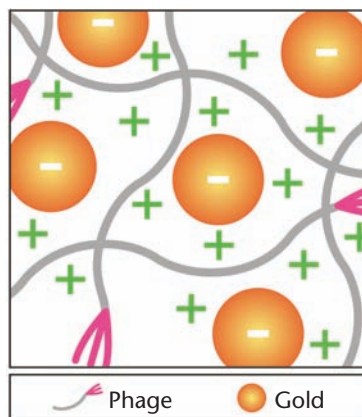


Figure 13.4 Au-phage networks. These multifunctional networks of gold combined with bacteriophages have the potential to target to the tumor vasculature and then be thermally ablated to treat the tumor. (Adapted from [42].)

sense, the physical (geometry) and chemical (surface functionalizations) features of the first-stage vectors are critical to improve the efficiency of any *in vivo* applications. In the following sections, we will outline a minimal array of methods to address the aforementioned tasks and methodically integrate the MDS system for any application that may be envisioned. Combining state-of-the-art microelectronics technology with finely controlled electrochemical etch, we developed protocols for the high-throughput manufacturing of highly reproducible PSPs: the first-stage vector (Figure 13.5). The objective of this chapter is to succinctly outline and describe validated techniques and protocols enabling the use of the MDS and to allow the successful reproduction of the results obtained. First, it is necessary to describe the typical protocols employed to microfabricate the first stage vectors (Figure 13.6). Briefly, in order to produce PSPs of a well-determined shape, desired pore size, and porosity, a silicon wafer is initially patterned with the desired two-dimensional shape, through standard lithographic techniques. The wafer then undergoes anodic etch in an aqueous solution of hydrofluoric acid. Controlling the parameters of the anodic etch determines the pore size and porosity of the material. Finally, the PSPs are released from the bulk silicon wafer by means of sonication in isopropanol solution. Several techniques can be employed to modify the surface of the PSPs. We describe how to oxidize the PSPs and then modify them with APTES (3-aminopropyltriethoxysilane) and with fluorescent dyes. Control of the proper surface modifications, quantification of the number of PSPs, and characterization of the overall size distribution are critical to properly reproduce experiments and ensure homogeneity within the PSPs. The techniques described take advantage of a:

1. ZetaPals Zeta Potential Analyzer to evaluate surface charge;
2. Beckman Coulter Counter to count and provide the size distribution of the PSPs [43];
3. Inductively Coupled Plasma-Atomic Emission Spectroscopy (ICP-AES) [44] to determine the degradability of the PSPs by quantifying the amount of silicon in the solution;
4. Becton Dickinson FACSCalibur to determine the size, shape, and fluorescence intensity emitted from the PSPs themselves or from any second-stage NP that might have been embedded within.

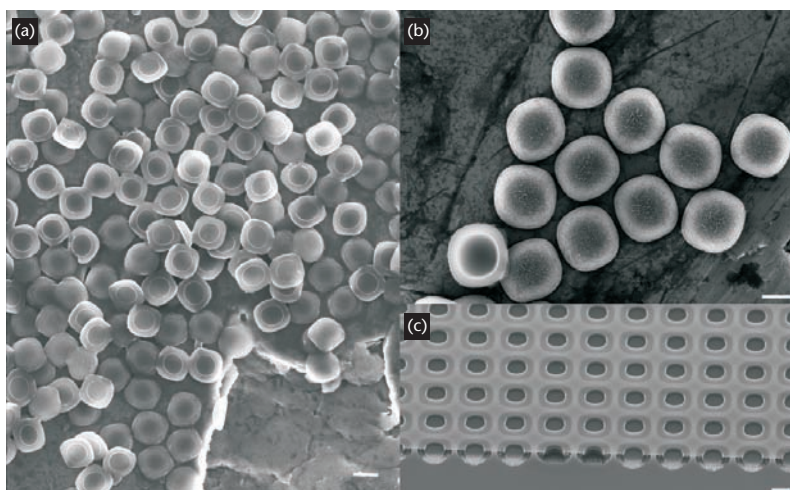


Figure 13.5 SEM micrographs of collections of porous silicon particles. (a) Overall view of a large cluster of large pores porous silicon particles after release showing substantial size and shape uniformity. (b) Close-up view of a small cluster of small pore porous silicon particles after release showing size and shape uniformity. (c) 45° tilt view of large pores porous silicon particles before release, showing substantial size and shape uniformity. The silicon nitride sacrificial layer is present on the sub-

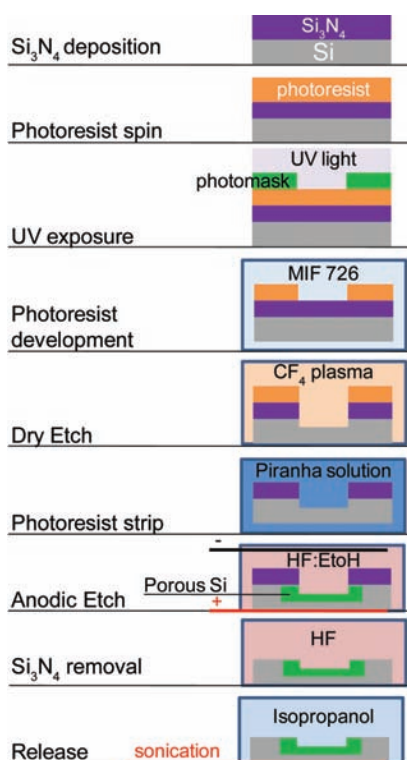


Figure 13.6 Schematic representation of the protocol steps necessary to fabricate pSi particles.

We also describe the protocols used to determine the loading and release kinetics of the PSPs and to quantify the amount of second-stage NPs loaded in or released from the pores of the PSP. We believe that, by the end of this chapter, the reader should be able to

fabricate, modify, and characterize the first-stage vectors and to control the loading and release of any second-stage NPs of choice.

13.2 Fabrication of PSPs

13.2.1 Materials

The entire process is performed in a cleanroom facility with the minimum requirements of:

- Furnace for the deposition of SiO_2 .
- Low pressure chemical vapor deposition (LPCVD) furnace for the deposition of Si_3N_4 .
- Photolithography tools (HMDS oven, spin coater, mask aligner, and so forth).
- White light ellipsometer, or any other tool to measure thin film thickness.
- Reactive ion etch (RIE) tool for the dry etch of Si_3N_4 , SiO_2 , and Si. CF_4 , SF_6 , and HBr gases have been employed in the protocol.
- Aluminum sputtering tool.
- Acid hood.
- Solvent hood with sonic bath.
- Wafer rinsing and drying tools.

The protocol uses two quartz/Cr dark field photolithographic masks with $2\text{-}\mu\text{m}$ circles patterned with $2\text{-}\mu\text{m}$ pitch, custom ordered from Photosciences, California.

The 100-mm heavily doped p-type silicon wafers with resistivity lower than $0.005\ \Omega\text{-cm}$ have been used. This material allows for the formation of pores in the range of a few nanometers to few hundred nanometers, depending on the details of the anodic etch. The use of P-type Si of different resistivity or of distinct n-type Si wafers grants access to other ranges of pore size and porosities, as described in Table 13.1.

The anodic etch solution is composed of 49% hydrofluoric acid (HF) and absolute anhydrous ethanol (EtOH). The ratio of HF to EtOH and the applied current density are crucial in determining the pore size and porosity of the PSPs.

The anodic etch is performed in a custom-made HF resistant tank, schematized in Figure 13.7. The most important features of this chamber are:

Table 13.1 Range of Accessible Pore Size Depending on Si Doping Type and Concentration

Wafer Type (Dopant Concentration)	Pore Range	Illumination [*]
p-type (<1015)	> 1 mm	N/A
p-type (1015–1018)	1–10 nm	N/A
p+-type (>1018)	10–100 nm	N/A
n-type (<1018)	10 nm–10 mm	No
n-type (<1018)	50 nm–10 mm	Yes
n+-type (>1018)	10–100 nm	No
n+-type (>1018)	50 nm–10 mm	Yes

^{*} Illumination refers to the ability to irradiate the front side of the wafer with light during the anodic etch process.

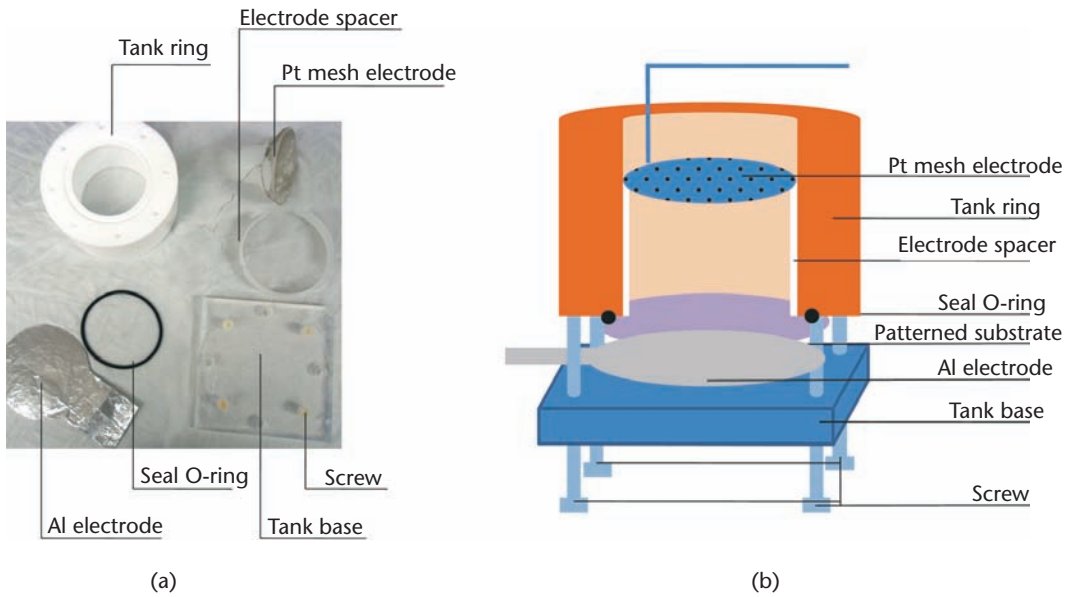


Figure 13.7 View of the anodic etch tank. (a) Disassembled view of the tank components. (b) Schematics of the assembly of the components.

- The ability to provide adequate backside electrical contact for the Si wafer. The backside contact must not be exposed to the etch solution. The backside contact is typically provided through thin aluminum foil, shaped as the wafer. Thus, the tank must provide enough mechanical stability to guarantee a uniform contact between the aluminum foil and the backside of the Si wafer.
- The ability to immerse a mesh electrode, facing the wafer and parallel to the wafer, at a fixed, replicable distance. The mesh electrode is usually constituted of Pt, an HF-resistant metal with sufficiently good electrical properties.
- The ability to expose a majority of the front side surface of the Si wafer to the etch solution, in order to maximize the yield of each etch process.
- The ability to resist acid attack by HF; Teflon and aluminum oxide are the materials of choice for the realization of the tank.
- The ability to allow for the escape of gaseous species formed during the etch process. The tank must have an opening from which the gas can escape, and if the Pt mesh is positioned horizontally, the gas bubbles must be able to escape between the grid.

A constant current power supply capable of currents up to 8A is required.

Chemicals:

- AZ-5209 photoresist, or equivalent positive, thin photoresist is required for photolithography.
- Isopropanol is required for the conservation of the PSPs following their release.
- 49% HF is required for the etch solution.
- Anhydrous 200-proof EtOH is required for the etch solution.
- Acetone, methanol, and isopropanol are required to clean the substrates.

Characterization:

- Scanning electron microscope with 0.5-nm resolution;
- Nitrogen absorption analysis tool (Quantasorb 3 from Quantachrome).

13.2.2 Methods**13.2.2.1 Thin Film Deposition**

The thin film deposition provides a masking layer to the Si wafers, necessary for the patterned anodic etch.

1. A 100-nm Si wafer (substrate) is stripped of eventual organic contaminants in 2:1 $\text{H}_2\text{SO}_4:\text{H}_2\text{O}_2$ piranha solution in an acid hood.
2. The wafer is rinsed for 5 minutes under flowing deionized water, spin dried.
3. The wafer is transferred to a carrier boat for oxide growth. The boat is placed at the center of an open furnace tube. Dry air is flowed into the furnace; the temperature is raised to 1,000°C and left there for 40 minutes, growing 50 nm of gate oxide. The exact thickness of the oxide layer is measured and recorded in a white light ellipsometer.
4. The substrate is transferred to the LPCVD furnace; the wafer is placed in the center of the loading boat and two dummy wafers are disposed on each side to guarantee uniformity of the resulting thin film. Si_3N_4 is deposited to reach the thickness of 80 nm, usually requiring 25 minutes of deposition. The exact thickness of the nitride layer is measured and recorded in a white light ellipsometer. Knowledge of the nitride thickness is necessary to properly time the dry etch step.

Guidelines

The uniformity of the thin film layer is the most important aspect of this step. Layers of uniform thickness (within a 5% maximum variation) are necessary for the success of the protocol, although 1% uniformity is generally preferred. To ensure the best possible uniformity, the substrate must always be carefully placed on the boat, in the center of the furnace, where the temperature is most uniform. The substrate must face away from the gas source and be surrounded by as many dummy wafers as possible.

13.2.2.2 Photolithography

The photolithography transfers the desired 2- μm holes pattern on the photoresist layer on top of the substrate. The patterned photoresist acts as masking layer for the dry etch.

1. The substrate is coated with HMDS to improve photoresist adhesion in an HMDS oven for 5 minutes.
2. AZ-5209 positive photoresist is spun on the substrate using: 500 RPM speed, 1,000 RPMS acceleration for 5 seconds, followed by 5,000 RPM/4,000 RPMS/30 seconds, resulting in a resist thickness of approximately 700 nm.
3. The photoresist is soft baked for 8 minutes in an oven at 90°C.
4. The 2- μm pattern is transferred from the photomask to the photoresist using a Karl Suss MA6 Mask Aligner, 70J exposure (approximately 3 seconds) using soft vacuum contact.

5. The transferred pattern is developed in an MIF 726 developer for 20 seconds, and then inspected for uniformity under a 100× optical microscope.
6. If the pattern is sufficiently uniform, the substrate is hard baked for 8 minutes in an oven at 120°C, to completely crosslink the photoresist.
7. If the pattern is not sufficiently uniform, the photoresist can be removed with acetone under sonication. The acetone residues can then be cleaned by subsequent rinses in methanol and isopropanol. The protocol can then be resumed from point 2.

Guidelines

The uniformity of the pattern is the most important aspect of this step. Even if a small portion of the substrate is not properly exposed, the substrate should be reprocessed. To obtain the best possible uniformity, it is critical to know the UV light source power for the aligner, which would allow for one to calculate the exposure time necessary to obtain the correct exposure. Since the source power cannot be measured, the best practice is to initially calibrate the exposure/development times on several dummy Si wafers, spun with photoresist, and use the best obtained parameters to pattern the substrate.

13.2.2.3 Dry Etch

The dry etch transfers the desired micrometric pattern from the photoresist to the silicon. This allows the patterned anodic etch to take place.

1. The substrate is transferred in a plasma etch tool, with the patterned side exposed to the plasma, where it undergoes the dry etch processes necessary to form a 200-nm trench into the Si by means of a 4-minute CF₄ etch (25 sccm, 200 mTorr, 250W in a Plasmatherm RIE).
2. The substrate is flipped to expose the backside (unpatterned) to the plasma. A 4-minute CF₄ etch (25 sccm, 200 mTorr, 250W in a Plasmatherm RIE) is employed to expose the bare silicon on the backside and ensure electrical contact for the successive anodic etch.

Guidelines

The timing and chemistry of the dry etch to obtain the desired trench depth and profile is the crucial aspect of this step. Each tool and etch chemistry will have their specific etch rate for Si₃N₄ and Si. Using the previously calculated thickness of the Si₃N₄ layer, it is possible to estimate the correct etch time (in seconds) necessary to form the 200-nm trench into the silicon, simply employing:

$$t = R_{Si_3N_4} \cdot h_{Si_3N_4} + R_{Si} \cdot 200 \tag{13.1}$$

where $R_{Si_3N_4}$ is the etch rate for Si₃N₄ in nanometers per second, $h_{Si_3N_4}$ is the thickness of the Si₃N₄ sacrificial layer in nanometers as measured by ellipsometry, and R_{Si} is the etch rate for Si in nanometers per second.

13.2.2 Anodic Etch

The anodic etch selectively porosifies the substrate where the silicon is directly exposed to the HF solution, forming PSPs.

1. The patterned substrate is stripped of photoresist and organic contaminants in 2:1 $\text{H}_2\text{SO}_4:\text{H}_2\text{O}_2$ piranha solution for 8 minutes.
2. A 200-nm thin film of sputtered aluminum is deposited on the nonpatterned backside of the substrate to improve electrical contact. The sputtering is performed for 12 minutes in a 16-wafer holding Varian sputter.
3. The etch tank is assembled as follows (Figure 13.8):
 - i. The tank ring is placed upside down, and the wafer is placed on top of the tank ring, sitting on the seal o-ring, with the patterned side facing inside the ring, where the solution will be poured.
 - ii. The aluminum-covered backside of the substrate is placed in conformal contact with an aluminum foil shaped like a table tennis racket.
 - ii. The base of the tank is screwed to the tank ring, ensuring sealing of the tank and providing the pressure necessary to guarantee the electrical contact between the substrate and the aluminum foil. The handle of the aluminum foil racket is now outside the tank and provides the contact spot to connect to the power supply.
 - iv. The tank is flipped back in the upright position and the platinum mesh is inserted at a distance of approximately 2.5 cm. An annular Teflon spacer positioned between the wafer and the platinum mesh determines the distance.
 - v. The etch solution, specified in Table 13.2, is poured in the etch tank.
 - vi. The anode (positive lead) of the power supply is connected to the aluminum electrode.
 - vii. The cathode (negative lead) of the power supply is connected to the platinum mesh electrode.

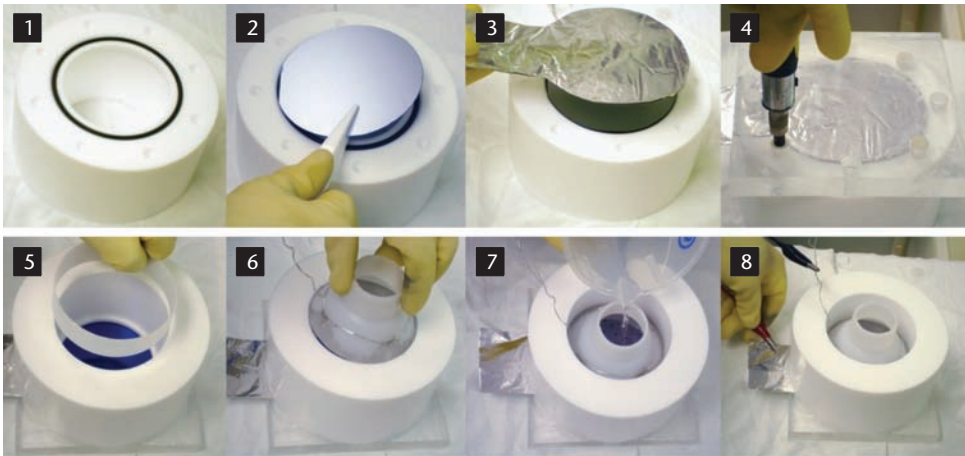


Figure 13.8 Assembly of the etch tank. (1) Upside-down view of the etch ring with seal o-ring mounted. (2) The substrate is placed on top of the o-ring seal with the nonpatterned backside facing outside the ring. (3) The aluminum electrode is placed on top of the substrate backside to provide electric contact. (4) The etch tank bottom, placed on top of the aluminum electrode, is screwed together with the tank ring to ensure electric contact and seal the tank. (5) The tank is flipped upright and the mesh electrode spacer is inserted in the etch ring. (6) The Pt mesh electrode is inserted in the etch ring. (7) The $\text{HF}:\text{EtOH}$ solution is poured in the etch tank. (8) The anode is connected to the aluminum electrode and the cathode to the platinum mesh electrode.

4. The current is started with the porosification current density and time specified in Table 13.2, to produce PSPs with size, pore size, and porosity specified therein. The current density is then raised to the release current density value and time specified in Table 13.2, forming the release layer.

Guidelines

This is the most important step of all, where the PSP and the release layer are formed. The choice of the correct current density will produce PSPs with the desired pore size and porosity. Additionally, another critical factor is the current density of the release layer. If set too high, the elements will release in the etch solution and be lost; if set too low, the elements will not release from the substrate and be unusable.

13.2.2.5 Release of pSi Elements to Obtain PSPs of Desired Shape/Size/Pores

1. The etch tank is emptied of the etch solution.
2. The tank is rinsed three times with deionized water to reduce HF concentration.
3. The tank is disassembled and the substrate removed.
4. The substrate is rinsed for 5 minutes under running deionized water to completely remove any HF residues.
5. The substrate is spin dried.
6. The substrate is then inspected visually under a 100× optical microscope. A golden-yellow color of the substrate indicates the successful formation of the porous elements. Observing yellow/purple circles of the appropriate diameter (2 μm) surrounded by a yellow colored corona under the optical microscope is also an indication of the successful formation of the porous elements.
7. The substrate is soaked for 30 minutes in HF to strip the SiO₂ and Si₃N₄ layers. Incomplete removal of these layers will prevent the release of the elements from the substrate and/or cause shattering of the elements.
8. The substrate is rinsed for 5 minutes under running deionized water to completely remove HF residues.
9. The substrate is spin dried.
10. The substrate is inspected visually. A dull yellow-grayish tint is a positive predictor for the element release from the substrate. A yellow-golden tint as in the previous inspection is a negative predictor for the element release. Under a 100× optical microscope a grey/purple tint is a positive predictor for the element release, while a yellow/purple tint is a negative predictor for the element release.

Table 13.2 Anodic Etch Parameters Used to Obtain Desired Pore Size

Target Pore Size	Etch Solution (HF:EtOH)	Etch Current Density (A/cm ²)	Etch Current Time (Seconds)	Release Solution (HF:EtOH)	Release Current Density (A/cm ²)	Release Current Time (Seconds)
6 nm	1:1	0.0129	110	2:5	0.779	6
15 nm	1:3	0.0390	90	1:3	0.620	6
26 nm	1:3	0.0900	45	1:3	0.620	6

Current densities are measured on the effective area of Si exposed to the etch solution.

11. The substrate is transferred to a crystallization dish filled with 40 ml of isopropanol.
12. The crystallization dish is placed in a sonication bath until the release of the elements, typically 1 minute. The occurred release can be visually determined by a subtle change in tint of the substrate, from grayish/green to shiny gray.
13. After release, the substrate is again inspected under a 100× optical microscope to determine release efficiency. The presence of dull gray disks of approximately twice the diameter of the original lithographic pattern indicates a released element. The presence of gray/purple or yellow/purple disks indicates nonreleased PSPs.
14. The isopropanol suspension rich in PSPs is then transferred in a 50-ml centrifuge tube and stored at 4°C.

13.2.2.6 Scanning Electron Microscopy (SEM) Characterization

A small aliquot of the PSP-rich suspension is spotted on a 17-mm SEM stage. The isopropanol is allowed to dry and the sample is analyzed in a scanning electron microscope. Cross-sectional views of the PSPs can be obtained, cleaving the substrate before releasing the PSPs and mounting the substrate piece on a 45° or 90° SEM stage.

13.2.2.7 Nitrogen Absorption/Desorption Characterization

A suspension containing 10 mg of PSPs (corresponding approximately to the product of 10 substrates) is centrifuged until the PSPs form a pellet at the bottom of the centrifuge tube, and all but 10 ml of the supernatant is removed; the PSPs are resuspended. The suspension is transferred to a nitrogen absorption analysis cuvette and dried completely. The cuvette containing the PSP powder is mounted on a nitrogen absorption analyzer and the absorption/desorption curves are collected. Using the provided software, the average pore size, the pore distribution, and the porosity for the analyzed PSPs are obtained by means of the Barret-Joyner-Halenda (BJH) model.

13.2.3 Characterization

The PSPs resulting from the described protocol are shown in Figure 13.9. The PSPs are analyzed by SEM to inspect their overall features and when using the standard. The 2- μm photolithographic pattern will result in quasi-hemispherical PSPs of 3.2- μm diameter and 1- μm height. The top side of the PSP, from where the porosification began, is characterized by a circular nucleation site, surrounded by an external corona. Pores run perpendicular to the nucleation site surface and parallel to the external corona surface (Figure 13.9). The nucleation layer, which extends 10–20 nm below the nucleation site, is constituted of pores with 2–3 nm in diameter. Right below the nucleation layer, the pore size rapidly increases to the one determined by the anodic etch parameters. The bottom side of the PSP is bowl-shaped and the pores are normal to the surface and have the characteristic size imparted by the anodic etch.

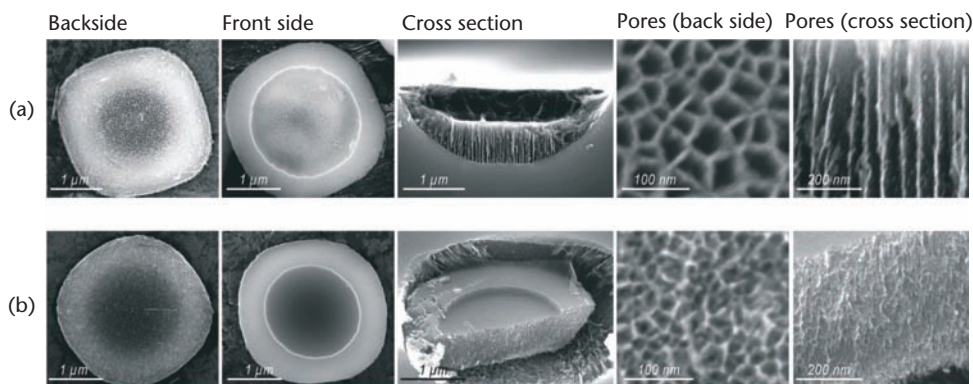


Figure 13.9 SEM images of PSPs. (a) Fabricated according to the parameters in the last row of Table 13.2. (b) Fabricated according to the parameters in the first row of Table 13.2. The front side shows the circular nucleation site surrounded by the external corona. The cross section shows the pores directionality from the nucleation site to the particle back side. (Reproduced with permission from [29] courtesy of Nature Publishing Group.)

13.3 Oxidation and Surface Modification with APTES of PSPs

13.3.1 Reagents

- Deionized (DI) water;
- IPA;
- Hydrogen peroxide (H_2O_2);
- Concentrated (95–98%) sulfuric acid (H_2SO_4);
- 3-aminopropyltriethoxysilane (APTES).

13.3.2 Methods

13.3.2 Wet Oxidation of PSPs

1. PSPs in isopropyl alcohol (IPA) (or any other organic media in which the PSPs are suspended) are dried in a glass beaker, on a hot plate (80°C – 90°C) in a fume hood. The smallest amount of liquid is desirable for this step, as this reduces the drying time for the process.
2. A piranha solution consisting of 1 volume of H_2O_2 and 2 volumes of H_2SO_4 is used for the wet oxidation of the PSPs. H_2O_2 is added to the dried PSPs and sonicated. Owing to the hydrophobicity of the silicon, the PSPs normally tend to float. Concentrated (95%–98%) H_2SO_4 is then added slowly to this solution.
3. The PSP suspension is then heated to 100°C – 110°C for 2 hours with intermittent sonication in a bath sonicator to disperse the PSPs. Utmost precautions should be taken during these steps, and the process should be carried out in a fume hood. Sonication helps not only in dispersing the PSPs but also in dislodging any air pockets within the pores of the PSPs.
4. The particulate suspension is then transferred to centrifuge tubes, and the PSPs are spun down at $\sim 3,000g$. The supernatant is discarded and the PSPs are resuspended in deionized (DI) water and transferred to microcentrifuge tubes and spun down again.

This process is referred to as washing the PSPs and is critical for the proper removal of any unreacted substrates. In this way the PSPs are washed five to six times in DI water until the pH of the suspension is approximately around 5 to 6. PSPs may then be transferred to an appropriate buffer (if used immediately) or sorted in IPA or DI water and refrigerated at 4°C until further use.

13.3.2.2 Surface Modification of PSPs with APTES

1. PSPs that are oxidized by the piranha method are washed thoroughly in water and then washed in IPA three to four times. After the washings, PSPs are resuspended in IPA.
2. PSPs are then transferred to a solution of IPA containing 0.5% (v/v) of APTES for 45 minutes to 2 hours, at room temperature. The PSPs are sonicated intermittently in a bath sonicator and placed on a tabletop shaker for the duration of modification.
3. The chemical modification is usually performed in a microcentrifuge tube. The reaction volumes used are below 0.8 ml. The lower volumes are ideal for the modification of micron-sized PSPs, as this consumes lower reagents during the modification and subsequent washing steps.
4. The PSPs are washed with IPA four to six times as described earlier and stored at 4°C. Alternatively, aliquots can be taken, dried, and stored under vacuum and desiccant until further use.

Figure 13.10 shows the schematic of the surface modification by the APTES

Useful Tip: It is difficult to spin down PSPs in aqueous media completely; most PSPs tend to stick to the walls of the tube or remain in suspension. This leads to huge losses of PSPs, especially if they undergo several cleaning steps to remove suspending media or reactants. In order to recover the maximum amount of PSPs during the centrifugation step, adding a small amount of detergent (like TritonX-100) assists in the formation of a nice PSP pellet. Typically 1–2 μl of 1% TritonX-100 in 300–600 μl of aqueous media should do the trick.

Make sure that the Triton is removed before proceeding to any further work with the PSPs. This is normally done by removing the supernatant after the PSPs have been spun down and then adding media to the pellet slowly, attempting not to disturb the PSPs. The PSPs are spun down again, the supernatant is discarded, and fresh media is added again. This can be done two to three times, depending on the discretion of the researcher.

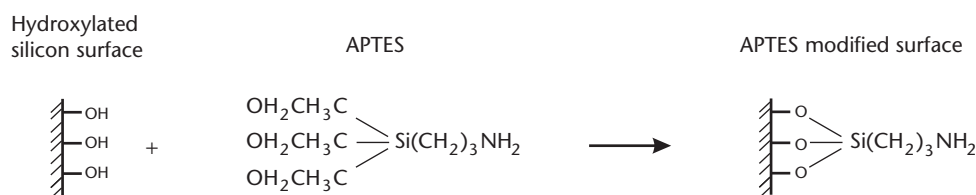


Figure 13.10 Schematic showing the modification of silicon surface with 3-aminopropyl triethoxy silane (APTES).

13.4 Fluorescent Dye Conjugation of PSPs

PSPs modified with APTES can be conjugated with any commercially available fluorescent dyes that have a hydroxy-succinimidyl ester (NHS) conjugated to them. The NHS ester readily reacts with primary amines. NHS conjugated dyes are commonly used to tag proteins and antibodies and can be purchased from Invitrogen and Pierce.

13.4.1 Reagents

- 10 mM Phosphate buffer (PB);
- pH~ 7.3 (for the conjugation);
- 1% Triton X-100 (for washing unconjugated dye).

13.4.2 Methodology

1. The APTES-modified PSPs are washed and suspended in the conjugation buffer.
2. The fluorescent dye to be conjugated is dissolved in the buffer and mixed with the PSP suspension.
3. The mix is sonicated and reacted for up to 1 hour. (The conjugation protocol provided by the supplier can also be followed.)
4. After reaction the PSPs are washed three times in 1% TritonX-100 followed by five to six washes in PB.

13.5 Zeta Potential Measurement

13.5.1 Equipment

- ZetaPals Zeta Potential Analyzer (Brookhaven Instruments Corp., Southborough, Massachusetts)

13.5.2 Reagents

- 10 mM Phosphate buffer (PB);
- pH~ 7.3 (for suspending the PSPs for performing the Zeta potential measurements).

13.5.3 Methodology

1. The application window for the zeta potential measurement (ZetaPals) is opened in order to power on the laser. After 15 minutes (for laser warm-up), the zeta potential measurements can be done.
2. The cuvette for holding the particulate suspension is rinsed with filtered (0.2 μm filter) buffer. The cuvette is filled with 1.5–2 ml of buffer. A small amount of PSPs is suspended in the buffer and well mixed either using a pipette or a brief sonication.
3. Make sure the electrodes are cleaned and rinsed with the buffer in which the measurements are performed.
4. After the electrodes are placed in the cuvette, the measurement for the zeta potential is started.

5. Typically, three runs of 25 cycles per run are performed, but for more consistent results during each run, the number of cycles can be increased based on the discretion of the user.
6. The counts per second (cps) during data acquisition should be above 20 Kilo counts per second (Kcps), and below 700 Kcps. The instrument will automatically register if the quality of the sample for measurement is good or bad.
7. A detailed explanation of operating the equipment can be found in the manual of the instrument or from a training session with a Brookhaven Instruments scientist.

13.5.4 Results

After oxidation the PSPs charge is negative. The negative charges depend on the number of hydroxyl groups that are formed on the surface of the PSPs. After modification with APTES, the PSPs become less negative due to the surface coverage by the silane. A complete multilayer APTES coverage leads to PSS with higher positive Z-potential.

Table 13.3 shows the typical results of zeta potential measurement on PSPs.

13.6 Count and Size Analysis of PSPs

13.6.1 Materials

13.6.1.1 Reagents

1. ISOTON II Diluent (Beckman Coulter);
2. Accuvettes (Beckman Coulter);
3. Standard cuvette (VWR);
4. 10-mL syringe (BD);
5. Single-use 0.20 mm syringe filter (Sartorius Stedim Biotech).

13.6.1.2 Facilities/Equipment

1. Z2 COULTER COUNTER Cell and Particle Counter (Beckman Coulter);
2. PC Computer with AccuComp Software (Beckman Coulter);
3. 50 μm Ampoule Aperture Tube (Beckman Coulter);
4. Sonicator (Branson).

13.6.2 Methods

1. 20 mL of ISOTON diluent into a CLEAN Accuvette.
2. Aliquot filter the ISOTON.
3. Clean a cuvette using 1 mL of the filtered ISOTON to remove dust/debris inside of the cuvette.
4. Aliquot 2 mL of filtered ISOTON into the clean cuvette.

Table 13.3 Zeta Potential of PSPs as Measured in 10 mM PB

PSP Sample	Zeta Potential (mV)
Oxidized PSPs	From -29 to -34
APTES PSPs	From +5 to +11

5. Using a concentrated sample of PSPs, aliquot a small volume (between 0.5 to 4 μL) into the cuvette (concentrated samples are usually in the range of 2×10^8 particles/mL).
6. Sonicate cuvette to ensure homogeneity within sample.
7. Touch SETUP on the control panel of the Z2.
8. Place sample into machine for measurement. Do not allow the probe to go all the way to the bottom of the cuvette. The cuvette is placed onto an Accuvette cap so that the probe can reach the sample.
9. Adjust and examine the “Aperture Viewer” so that during the experiment one can observe any possible blocking of the aperture.
10. Input the upper and lower size limits:
 - i. For 3.2 mm PSPs (seen as 2 μm): 1.1–2.8 μm .
11. Touch SETUP again, scroll down to Optimize Settings, and move cursor to say YES.
12. Touch START/STOP and review settings.
13. Touch START/STOP again, and the Z2 should begin the measurement.
14. Observe the Concentration on the control panel of Z2; if it is too high, consider diluting the sample.
15. When the measurement is finished, import the run into PC using AccuComp software.
16. Inspect the graph for one central peak; then using the software, calculate the number of PSPs measured/counted.
17. Remove the sample, sonicate briefly, and repeat steps 7–16 four more times.
18. Average the counts and find the standard deviation.
19. To get to your overall count, multiply the number/mL of the measured sample by the dilution factors used when the sample was prepared.

Note: Each measurement can be further analyzed to give size distribution, overlaying runs, and averaging multiple runs into one file/graph. Furthermore, Beckman Coulter has recently released new counters called “Multisizers” that have aperture sizes that range from 20 to 2,000 mm and thus can count particles as small as 400 nm.

13.6.3 Data Acquisition, Anticipated Results, and Interpretation

When the sample is measured at the Z2 Analyzer, the resulting signal is calculated into the volume of diluent displaced per event. This gives an idea of the change in morphology of the particles over time and of the total number of readable particles present at each time point. Figure 13.11 is a sample Z2-generated graph using the AccuComp software. In this figure, we have the cell/particle diameter versus the number of particles counted per milliliter. One can move the cursor to whatever location to display the number of particles per milliliter at that particular volume; furthermore, one can select a whole area between two volumes to find the number of particles counted in that section. The six menu options at the top left-hand corner of the figure allows for the manipulation of items within the figure. Under the “Run File” menu, users can save graphs generated, add overlays, and export critical data to Excel. In “Graph,” users can customize the options displayed on the graphs from a pull-down menu with a list of possible x and y values. The “Analyze” menu allows the user several options to interpret the data

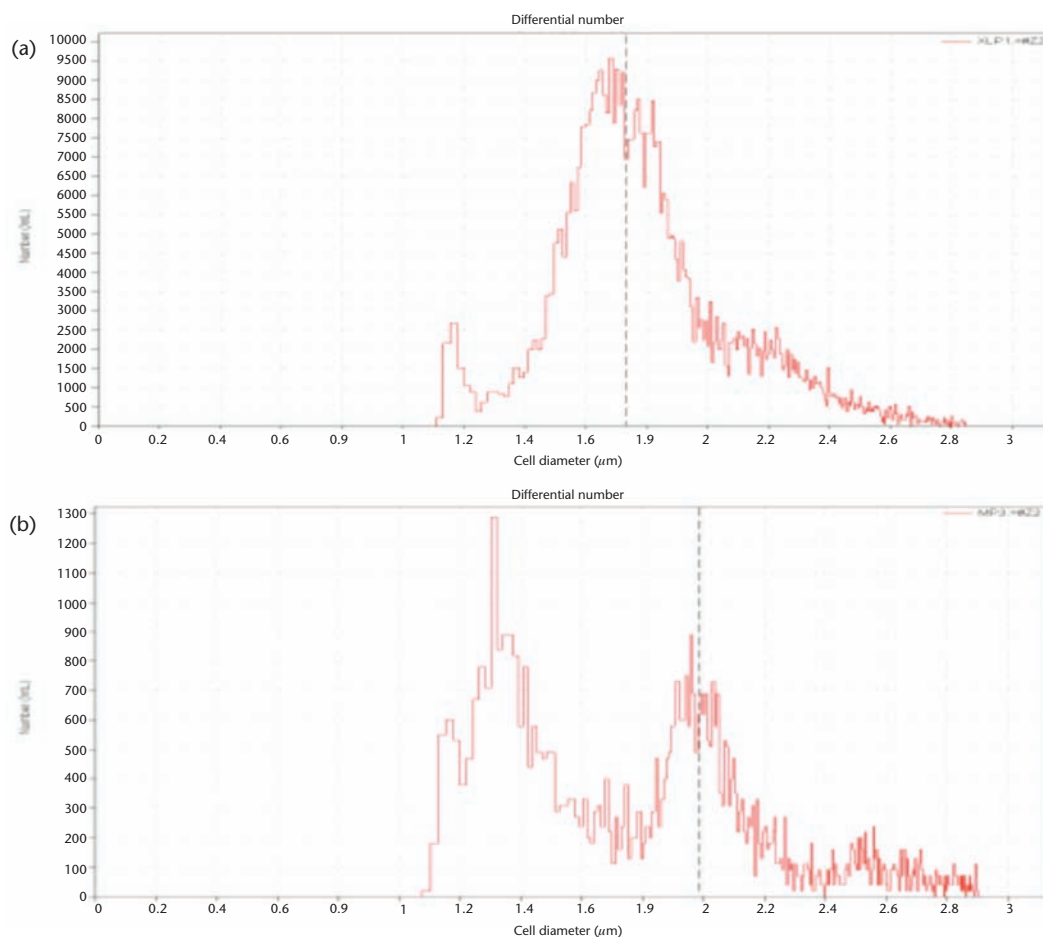


Figure 13.11 Graphs produced by AccuComp displaying the size distribution of a PSP. (a) Typical profile for vectors with extra large pores (60–80 nm). (b) Profile for vectors that have been broken; notice the typical peak at ~2 μm.

and determine the total number of particles counted and measured in that particular file.

13.7 Using Inductively Coupled Plasma–Atomic Emission Spectroscopy (ICP-AES) to Determine the Amount of Degraded Silicon in Solution

13.7.1 Materials

13.7.1.1 Reagents

1. 0.45 μm Nylon Filter Tubes (VWR);
2. 15 and 50 mL Polypropylene Conical Tubes (BD FALCON);
3. ISOTON II Diluent (Beckman Coulter);
4. Distilled H₂O;
5. Yttrium;

6. Silicon.

13.7.1.2 Facilities/Equipment

1. ICP-AES/OES (Varian);
2. Autosampler (Varian);
3. Argon Saturator Accessory (Varian, suggested).

13.7.2 Methods

1. Collect sample (i.e., 100 μL). Highly recommend collecting sample in triplicate.
2. Place sample into nylon filter tube.
3. Centrifuge sample at 4,200 rpm for 10 minutes.
4. Remove filter and collect the solution that flowed through.
5. Prepare a diluted sample to be analyzed by ICP.
 - i. For each individual sample, aliquot 5 mL of a solution that contains distilled water and 1 ppm of Yttrium into a 15-mL conical tube.
 - ii. Aliquot a known amount of sample from the flow through into the conical tube. Keep this amount consistent (i.e., 50 μL from the $\sim 100 \mu\text{L}$).
6. Prepare known concentrations of silicon “standards” with 1 ppm of Yttrium. Suggest preparing 0, 25, 50, 100, 250, 500, and 1,000 ppm solutions of silicon.
7. Briefly shake sample and silicon standards.
8. Load samples and standards in autosampler*.
9. Set up template for acquisition. ICP starts each run by running the known concentrations and finishes by running a calibration off one of the standards. Suggest using 50 ppm of silicon as the control calibration and rerun the known concentrations after 15–20 samples have been analyzed.
10. When all the samples have been measured, examine the data of each sample and, if necessary, mask any run that may have extremely high standard deviations.
11. Export data to Excel or any other spreadsheet application.
12. Analyze data to determine silicon concentration of samples.

*Note: It is highly advisable that the operation and measurement of samples using the ICP-AES/OES machine be done by an operator that is highly proficient in running the machine.

13.7.3 Data Acquisition, Anticipated Results, and Interpretation

13.7.3.1 Data Acquisition

The data received by the user will be in spreadsheet format, with the first row showing the data labels, as shown in Table 13.4.

Table 13.4 Data Labels for ICP Data

Tube	Sample Labels	Si 250.690	Si 251.432	Si 251.611	Si 288.158	Y 360.074	Y 371.029
------	---------------	------------	------------	------------	------------	-----------	-----------

The first column, “Tube,” designates in what rack and position (Rack:Position) within the autosampler the machine is measuring from. In this particular setup there are

two racks each with 60 positions available to hold the samples (racks 1 and 2) and a third rack that holds the known concentrations. The next column is the “Sample Label” that is used at the start of the experiment to designate what sample is being measured. The next four columns that start with “Si” correspond to the four wavelengths used to measure the concentration of Silicon within the sample. The last two columns are used to show the measurement of Yttrium within the sample. Yttrium measurement is important to assess the stability of measurements in time. The tool normalizes the Yttrium reading to 1.00 for the first sample in both wavelengths and then uses this value to calibrate for the decay in concentration found in the subsequent samples. Calibration to the Yttrium standard is crucial, since, depending on the number of samples, measurements can take up to several hours and may need to run overnight (60 samples take about 3–4 hours), and thus measurements would need to be adjusted for any decay in the readings.

Each sample will have its own row, including the known concentrations given in $\mu\text{g/L}$ (Table 13.5). The known concentrations are set to the actual value and are used to build a standard curve/line. The sample’s values are then extrapolated from the curve obtaining a numerical value. At the end of a cycle, the machine runs the calibration concentration, labeled as “Cont. Calib. Verif.,” to verify proper calibration. In this particular

Table 13.5 Actual Values from ICP-AES Analysis (in $\mu\text{g/L}$)

Tube	Sample Labels	Si 250.690	Si 251.432	Si 251.611	Si 288.158	Y 360.074	Y 371.029
3:1	Blank	0	0	0	0	0.8	0.9
3:2	Si Standard A	25	25.0000e	25	25	0.8	0.9
3:3	Si Standard B	100	100	100	100	0.8	0.9
3:4	Si Standard C	250	250	250	250	0.8	0.9
3:5	Si Standard D	500	500	500	500	0.8	0.9
3:6	Si Standard E	1,000	1,000	1,000	1,000	0.8	0.9
2:1	61	56.8	70.9	40.0	45.6	0.7	0.8
2:2	62	28.9	68.5	36.1	32.0	0.7	0.8
2:3	63	28.2	60.1 uv	36.3	31.2	0.7	0.8
2:4	64	65.2	64.6	69.7	62.3	0.7	0.8
2:5	65	55.5	77.6	49.4	53.2	0.7	0.8
2:6	66	55.1	50.1	50.7	45.1	0.7	0.8
2:7	67	42.2	42.6	55.9	50.5	0.7	0.8
2:8	68	51.9	60.0	37.7	44.9	0.7	0.8
2:9	69	30.4	63.4	43.6	33.8	0.7	0.8
2:10	70	73.3	84.4	72.3	68.2	0.7	0.7
2:11	71	55.2	75.5	57.8	53.4	0.7	0.7
2:12	72	24.4	28.1 uv	7.9	9.1	0.7	0.8
2:13	73	4.0	47.9	9.7	11.9	0.7	0.8
2:14	74	2.7	39.6 uv	15.6	12.6	0.7	0.8
2:15	75	7.0	67.8	29.6	29.3	0.7	0.7
2:16	76	22.0	27.3 uv	18.3	17.2	0.7	0.8
2:17	77	11.7	49.3	24.0	17.9	0.7	0.8
2:18	78	38.2	50.9	34.6	36.9	0.7	0.8
2:19	79	30.6	40.4	36.6	37.1	0.7	0.8
2:20	80	37.3	56.0	31.3	26.2	0.7	0.8
3:7	Cont. Calib. Verif.	49.5	72.1 Q	52.1	45.8	0.8	0.8

Values from acceptable wavelengths are in red.

example the reference sample is set to 50 ppm or 50 $\mu\text{g/L}$. Upon inspection of the sample data, some values are observed to have additional letters or even negative sign, such as Q, uv, and e. Q and uv are used to designate values that are found to be under detection limits. The operator designates the letter e to a particular value that had to be edited. This is preformed only when a value has an extremely high internal standard deviation, in an attempt to mitigate the effect of any stray data within the run of that particular sample.

13.7.3.2 Analyzing data

Only data from wavelengths for which the reference sample was measured within 10% of the actual value should be used for analysis. Inspecting the output file, it can be observed that a “Q” is placed next to any value in the control calibration row that does not fall within 10% of the known value of 50 $\mu\text{g/L}$. Thus, only wavelengths with a reference sample value between 45 and 55 $\mu\text{g/L}$ are used. The wavelength’s control concentration values are then rescaled such that the reference sample concentration measurement is set equal to the expected concentration of 50 $\mu\text{g/L}$. For example, if the control calibration sample value for a given wavelength were to be 48, then every value in the column would be multiplied by 50/48. Then using the resulting values that have been rescaled or normalized to a value of 50 from each sample and averaging with the other samples (since each sample was run in triplicate) will result in the final concentration of silicon of that particular sample in $\mu\text{g/L}$ (Table 13.6).

However, one still needs to account for the dilution factors involved in the preparation of the sample. Thus, the true concentration of silicon in the sample can be found multiplying by the dilution factor, as seen in (13.2):

$$\frac{V_{sol}}{V_{sample}} \times 2 \quad (13.2)$$

where

V_{sol} = volume of solution;

V_{sample} = volume of the sample.

Multiply by two, since we only used half of the sample to be measured.

This simple calculation provides the amount of silicon in your sample in $\mu\text{g/L}$.

Depending on the preference of the user, there are two alternative methods to interpret the results. The most beneficial, for most applications, is displaying the amount of silicon released into solution as a percentage of the total amount of silicon that can be released per PSP (Figure 13.12(a)). This type of interpretation facilitates the display of minor degradation rate changes within the different PSPs. Using this interpretation, PSPs that degrade quicker would show a steeper slant during their “linear” degradation. The other interpretation displays the total amount of silicon that is in solution (Figure 13.12(b)). This analysis would be useful in showing the different amounts of silicon contained in the different PSP types. Ideally, it would show that once degraded, PSPs with larger pores would release a lower amount of silicon in solution.

13.7 Using Inductively Coupled Plasma–Atomic Emission Spectroscopy (ICP-AES) to Determine the Amount of Degraded Silicon in Solution

Table 13.6 Normalized Values from ICP-AES Analysis

Tube	Sample Labels	Si 250.690	Si 251.432	Si 251.611	Si 288.158	Y 360.074	Y 371.029
3:1	Blank	0	0	0	0	0.8	0.9
3:2	Si Standard A	25	25.0000e	25	25	0.8	0.9
3:3	Si Standard B	100	100	100	100	0.8	0.9
3:4	Si Standard C	250	250	250	250	0.8	0.9
3:5	Si Standard D	500	500	500	500	0.8	0.9
3:6	Si Standard E	1,000	1,000	1,000	1,000	0.8	0.9
2:1	61	57.3	70.9	38.4	49.8	0.7	0.8
2:2	62	29.1	68.5	34.6	35.0	0.7	0.8
2:3	63	28.5	60.1 uv	34.8	34.1	0.7	0.8
2:4	64	65.8	64.6	66.9	68.0	0.7	0.8
2:5	65	56.1	77.6	47.4	58.1	0.7	0.8
2:6	66	55.6	50.1	48.6	49.3	0.7	0.8
2:7	67	42.7	42.6	53.6	55.1	0.7	0.8
2:8	68	52.4	60.0	36.2	49.1	0.7	0.8
2:9	69	30.7	63.4	41.9	36.9	0.7	0.8
2:10	70	74.0	84.4	69.4	74.5	0.7	0.7
2:11	71	55.7	75.5	55.5	58.4	0.7	0.7
2:12	72	24.6	28.1 uv	7.6	10.0	0.7	0.8
2:13	73	4.1	47.9	9.3	13.0	0.7	0.8
2:14	74	2.8	39.6 uv	15.0	13.7	0.7	0.8
2:15	75	7.1	67.8	28.4	32.0	0.7	0.7
2:16	76	22.2	27.3 uv	17.5	18.8	0.7	0.8
2:17	77	11.8	49.3	23.0	19.5	0.7	0.8
2:18	78	38.6	50.9	33.2	40.3	0.7	0.8
2:19	79	30.9	40.4	35.1	40.5	0.7	0.8
2:20	80	37.7	56.0	30.1	28.6	0.7	0.8
3:7	Cont. Calib. Verif.	50.0	72.1 Q	50.0	50.0	0.8	0.8

Values that have been normalized are in blue.

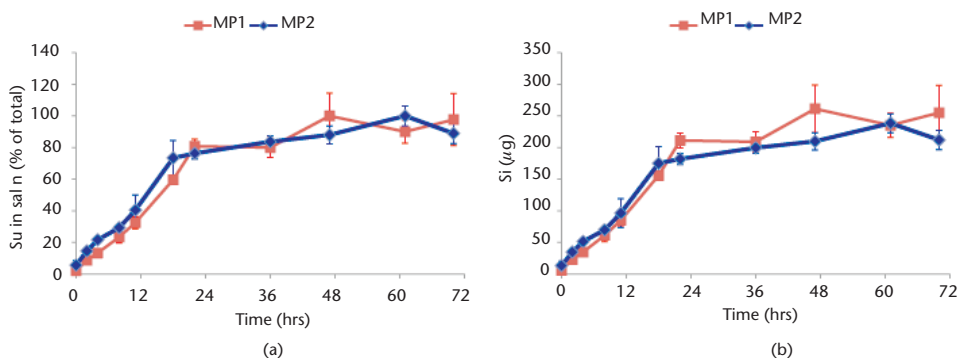


Figure 13.12 ICP graphs produced in Excel showing multiple ways to display the amount of silicon dissolved into the solution. MP1 and MP2 refer to a PSP of medium-sized pores with 10 and 15 nm, respectively. (a) Displaying the amount of silicon in solution by using the percentage of total possible silicon in solution. (b) Displaying the amount of silicon by showing the amount, by mass, of silicon.

13.8 Flow Cytometry to Characterize PSP Shape, Size, and Fluorescence Intensity

13.8.1 Materials

13.8.1.1 Reagents

1. Sodium chloride;
2. Distilled water;
3. Phosphate buffered saline, PBS pH 7.2 (Gibco);
4. 5-mL polystyrene round bottom tubes (BD Falcon).

13.8.1.2 Facilities/Equipment

1. FACSCalibur (Becton Dickinson, BD);
2. Computer running CellQuest software (Becton Dickinson, BD).

13.8.2 Methods

1. Start system. Power on Calibur, then computer.
 - i. Allow 15 minutes for machine to warm up in "STNDBY."
2. Mix 9g of NaCl into 100 mL of distilled water, thus 9% NaCl.
3. Make a 1:10 dilution of 9% NaCl in water (sheath fluid).
4. Load sheath fluid into proper compartment and empty out the waste, if necessary.
5. Set up acquisition parameters:
 - i. Parameters include detectors/amps, instrument settings, file names, location of saved file, compensation, and threshold.
 - ii. For particles only, see Table 13.7 for reference settings.
6. Prepare sample. Aliquot $\sim 5 \times 10^5$ PSPs into 500 mL of PBS into a polystyrene tube. We suggest to run the samples in triplicate, by either reading same sample three times or running three different samples each with at least 1×10^5 PSPs.
7. Briefly vortex sample.
8. Load polystyrene tube, press RUN, and select a flow rate:
 - i. LOW: 12 $\mu\text{L}/\text{min}$ (information obtained from the BD Web site on January 21, 2009);
 - ii. MID: 35 $\mu\text{L}/\text{min}$ (suggested to start here if using same concentration as above);
 - iii. HI: 60 $\mu\text{L}/\text{min}$.
9. After each sample, briefly run some distilled water through the machine until there are no events recorded in the acquisition plots.
10. Repeat steps 7–9 for each sample.
11. Analyze samples using CellQuest software.

Table 13.7 Recommended Instrument Settings for Particle Measurement

Detector	Voltage (V)	Mode
FSC	E-1	LOG
SSC	475	LOG
FL1	800	LOG
FL2	750	LOG
Threshold	Primary: FSC	30 (for other applications, leave at 52)
	Secondary: SSC	52

13.8.3 Data Acquisition, Anticipated Results, and Interpretation

The CellQuest software allows the user to customize the type of data that can be collected and displayed. Certain graphs can only be used for acquisition or analysis or for acquiring and analyzing (Acquisition → Analysis) the data simultaneously. The software is able to display data in five basic graphs: histogram, density, dot, contour, and 3-D plot. The first three can be set to Acquisition, Analysis or Acquisition → Analysis, while the last two, contour and 3-D plot, can only be used for the Analysis display and data should be acquired through other graphs (Figure 13.13). Histograms may also be overlaid, thus allowing users to compare several curves on the same plot.

Quantitative results from CellQuest can be obtained for histograms and regions (available in square, polygon, or circle) or gates of interest (both are manually drawn by user). Statistics are selected by choosing the appropriate type from the “Stats” pull-down menu located in the toolbar at the top of the screen. This results in an embedded box that can be resized or moved with the user-selected statistics inside. This box contains

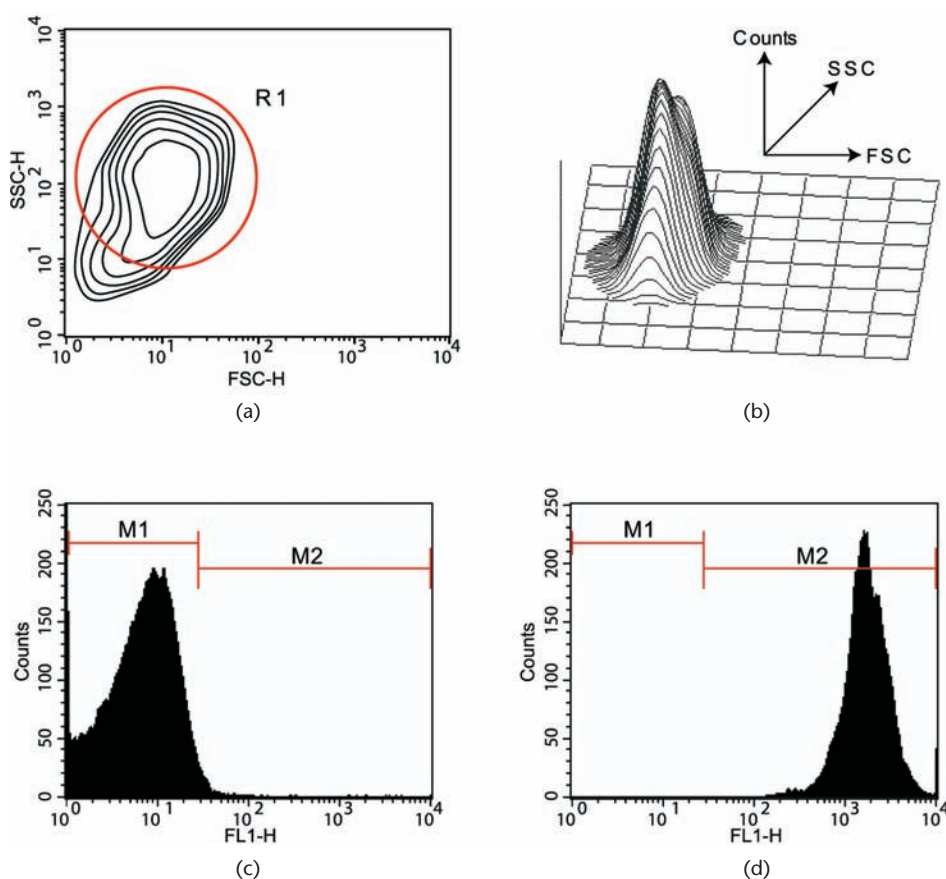


Figure 13.13 Using flow cytometry to study the PSPs' size and fluorescence. (a) Depicts the relative size (FSC) and shape (SSC) of the PSPs through a contour plot, Region R1 represents the gating region. (b) 3-D plot showing the distribution of PSPs gated in (a), where the z-axis represents the total number of counts/particles. (c) Histogram showing the background fluorescence of unloaded PSPs and is used to set up M1 so that at least 99% of events are captured here and M2 captures the rest, and (d) the increase in fluorescence distribution after loading the particles, keeping M1 and M2 regions the same as in part (c). (Reproduced with permission from [29] courtesy of Nature Publishing Group.)

several parameters including (but not limited to) mean, median, C.V., standard deviation, peak, total event, and events gated.

For the analysis of PSP shape and size, a bivariate plot (dot, contour, or density can be used) graphing forward scatter (FSC) versus side scatter (SSC) is used. This type of analysis can also be used to exclude events by defining a polygonal region of interest around the population of interest and analyzing the statistics within that region to obtain values for the geometric mean in both the X and Y parameters.

In addition, the FACSCalibur has the capabilities for fluorescence analysis. In relation to this procedure, only two colors will be described: FL1 (green) and FL2 (red). The green fluorescence (FL1) can detect FITC and QDot 525, as an example, using a 530/30 bandpass filter. The red fluorescence (FL2) can detect QDot 565 using a 575/26 bandpass filter. If single color detection is needed, color compensation can be set to zero. However, when detecting dual green-red color, FL1 compensation is set to 25% FL2, and FL2 compensation is set to 35% FL1 using the Compensation palette under the Cytometer pull-down menu in the CellQuest window.

This type of fluorescent setup allows users to characterize and quantify the amount of second-stage NPs loaded into the PSPs. To accomplish this, first the region of interest is located within a dot plot of FSC versus SSC. Then a histogram displaying the detector (FL1 or FL2) is created. This plot selectively displays the events within the defined region that correspond to the second-stage NP used.

13.9 Loading and Release of Second-Stage NPs from PSPs

13.9.1 Loading of NP into PSPs

13.9.1.1 Materials

Reagents

1. Nanoparticles (i.e., QDots, SWNT);
2. 1.5-mL low-binding polypropylene centrifuge tubes (VWR International);
3. DI water;
4. Tris(hydroxymethyl) aminomethane (Tris-HCl).

Facilities/Equipment

1. Thermo Scientific Barnstead LabQuake Tube Rotators (Thermo Scientific).

13.9.1.2 Methods

1. Put 3.0×10^5 PSPs in low-binding polypropylene tubes in 3 mL of DI water.
2. Adjust Tris-HCl to a pH of 7.3.
3. Add NPs and adjust the final solution to 20 mL using Tris-HCl (i.e., 2 mM QDots: 5 μ L Qdots + 3 μ L H₂O + 12 μ L Tris-HCl, or 20 ng/ μ L PEG-FITC-SWNTs: 9 μ L SWNTs + 3 μ L H₂O + 8 μ L Tris-HCl).
4. Incubate samples on tube rotator (~20 r.p.m.) for 15 minutes at room temperature.
5. Dilute samples with Tris-HCl to final volume of 150 μ L and measure fluorescence intensity using flow cytometry.

13.9.2 Release of NPs from PSPs

13.9.2.1 Materials

Reagents

1. Nanoparticles (i.e., QDots, SWNT);
2. 1.5 mL low-binding polypropylene centrifuge tubes (VWR International);
3. DI water;
4. Tris(hydroxymethyl) aminomethane (Tris-HCl);
5. Sodium chloride.

Facilities/Equipment

1. Thermo Scientific Barnstead LabQuake Tube Rotators (Thermo Scientific).

13.9.2.2 Methods

1. Combine 2.1×10^6 PSPs at pH 7.3 with a final solution of 140 mL:
 - i. $2 \mu\text{M}$ QDots in 200 mM Tris-HCl;
 - ii. $20 \text{ ng } \mu\text{L}^{-1}$ PEG-FITC-SWNT in 20 mM Tris-HCl;
 - iii. $1 \mu\text{M}$ QDots + $10 \text{ ng } \mu\text{L}^{-1}$ PEG-FITC-SWNT in 50 mM Tris-HCl.
2. Incubate samples on tube rotator (~ 20 r.p.m.) for 15 minutes at room temperature.
3. Wash samples in 1.4 mL of DI water.
4. Centrifuge for 5 minutes at 4,200 r.p.m.
5. Remove supernatant and resuspend in $70 \mu\text{L}$ DI water. Use $10 \mu\text{L}$ from each sample to assess fluorescence intensity using flow cytometry. Record intensity at time 0 and then over several time points (i.e., 30, 60, 90, 180, 360, 1,200 minutes).
6. Dilute residual $60 \mu\text{L}$ to 3 mL using 20 mM Tris-HCl 0.9% NaCl (release buffer).
7. Incubate at 37°C on tube rotator (~ 20 r.p.m.) for your defined amount of time.
8. After each time period has expired, centrifuge the sample for 5 minutes at 4,200 r.p.m. and measure fluorescence using flow cytometry.

13.9.3 Data Acquisition, Anticipated Results, and Interpretation

Determining the amount of agent that is loaded or released is critical for any delivery system. Proper characterization of the second-stage NPs is necessary for the optimal loading into the first stage vector. The knowledge of the second stage's surface charge, size, and concentration will greatly impact the choice of the pore size and surface charge of the first stage to be used to optimize the loading and release of these second-stage NPs (Figure 13.14). To characterize the first stage PSPs after they have been loaded and to determine the kinetics of second-stage NPs release both flow cytometry and confocal microscopy can be used. These are extremely useful tools when the loaded NPs are fluorescently tagged. Flow cytometry can characterize the amount of loaded NPs based on fluorescence intensity (Figure 13.15). To properly evaluate the amount of loaded NPs, it is necessary to compare two samples: PSPs with pores whose size will not allow the loading of the NPs (pore size too small), and PSPs with an adequate pore size to properly load the NPs of choice. This type of analysis allows for the discrimination of the amount

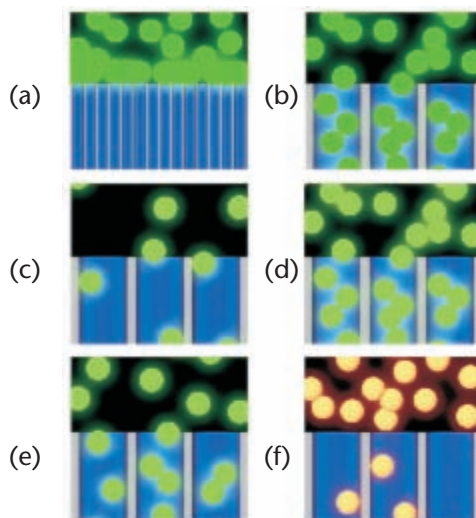


Figure 13.14 Models representing the three major mechanisms responsible for the optimal loading and release of second-stage NPs from PSPs. Size, dose, and charge are critical factors that govern the amount of NPs that can be loaded within the PSPs. Size dependency and the size of the pores determine the types of NPs that can be preferentially loaded in PSPs. (a) NPs that are too big remain outside. (b) NPs that are smaller than the size of the pores are loaded into the PSPs. Dose dependency: (c) a lower concentration of NPs in the loading solution results in reduced loading into the pores while (d) an increased concentration will result in increased number of NPs loaded within the pores. Charge dependency: (e) NPs with a surface charge opposite to PSPs are strongly attracted into the pores, while (f) NPs with a similar charge to that of the PSPs will result in NPs being partially or completely repelled from loading into the pores. (Reproduced with permission from [29] courtesy of Nature Publishing Group.)

of fluorescence that can be attributed to NPs adhering to the surface of the PSPs, and the fluorescence due to the NPs loaded inside the pores.

Confocal microscopy is useful in determining the distribution of the second-stage NPs within the first-stage PSPs (Figure 13.16) and in quantifying the amount of fluorescence attributed to the embedded NPs. However, a large sample population would be needed to get a statistically significant average intensity and thus flow cytometry would be more appropriate. The distribution of the NPs within the PSPs can be detected by simply zooming in on the PSP and then defining a ROI around that PSP. The next step is to draw an intensity profile/line covering the diameter of the PSPs, a graph that displays the intensity versus the length of the line is produced and showing the fluorescence intensity of the NPs distributed in the PSP. For example, when PSPs are loaded simultaneously with two types of NPs, it was concluded that the larger NPs were exclusively found in the central area of the PSP (associated with the larger pores), while smaller NPs were found throughout the entire vector but with a primary accumulation on the border of the PSP (associated with the smaller pores) (Figure 13.16).

The release of the NPs from within the pores of the PSPs can also be characterized using flow cytometry (Figure 13.15). This is achieved by indirectly measuring the residual fluorescence of PSPs after they have released the second stage NPs. Carefully choosing time points and displaying the data as percentage released of the optimal loading can give crucial data regarding the release kinetics from within the pores and thus assist in on the best choice of PSP characteristics needed for optimal delivery.

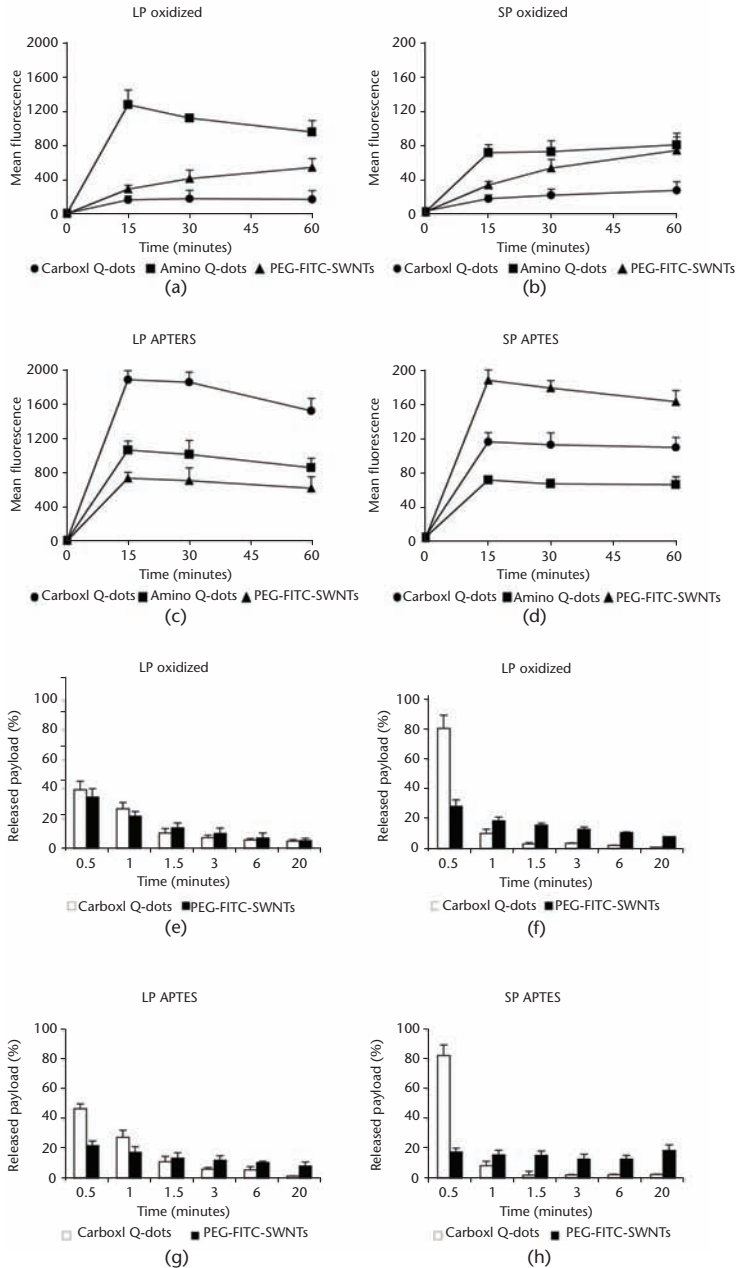


Figure 13.15 Loading and release of second-stage NPs from PSPs. (a–d) Four different types of PSPs were loaded with different second-stage NPs and their mean fluorescence measured by flow cytometry over time were measured: (a) LP oxidized, (b) SP oxidized, (c) LP APTES, and (d) SP APTES. (e) Release of Q-dots and PEG-FITC-SWNTs from LP oxidized, (f) SP oxidized, (g) LP APTES, and (h) SP APTES was measured over time and expressed as a percentage of the total amount of second-stage NP payload released from the PSPs for every time interval, after optimal loading. (Reproduced with permission from [29] courtesy of Nature Publishing Group.)

13.10 Discussion and Commentary

This chapter describes a novel multistage delivery system (MDS) based on PSPs capable of sequentially negotiating biobarriers and improve targeted delivery of imaging and

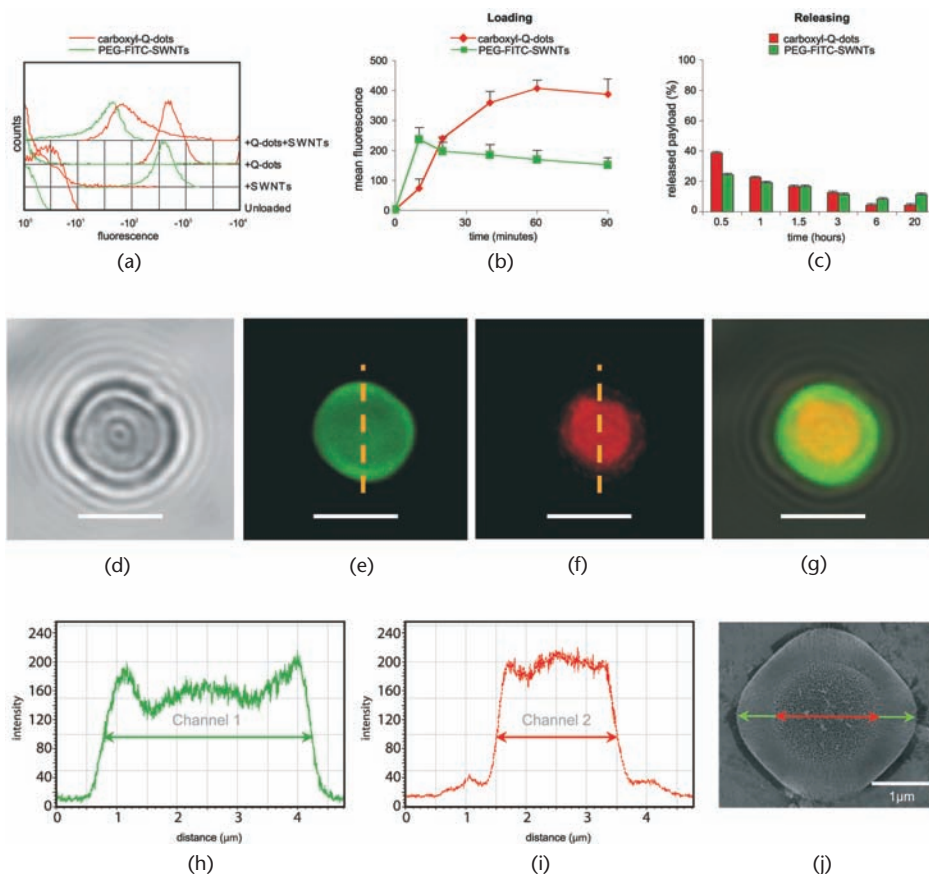


Figure 13.16 Simultaneous loading and release of Q-dots and PEG-FITC-SWNT. (a) FACS histogram-overlay of unloaded PSPs; PSPs loaded with PEG-FITC-SWNTs (+SWNTs), with Q-dots (+Q-dots) and with both Q-dots and SWNTs (+Q-dots +SWNTs). Flow cytometry analysis of (b) simultaneous loading and (c) release of second-stage NPs. (d–g) Confocal microscopy images show the localization of PEG-FITC-SWNTs (green) and Q-dots (red) in a single PSP: (d) bright-field, (e) green and red (f) fluorescence, and (g) overlay are shown. (h, i) Fluorescence intensity profiles of each channel along the orange dashed lines in (e) (PEG-FITC-SWNTs) and (f) (Q-dots) are shown, respectively. (j) The green and red arrows incorporated into the SEM image confirm the spatial distribution of fluorescence in the PSP. White scale bars in (d–g) are 3 μm . (Reproduced with permission from [29] courtesy of Nature Publishing Group.)

therapeutics. The versatility and ease of modification of the MDS are one of its major advantages over competing multistage delivery technologies. The methods previously outlined constitute the core of the MDS technology, but few crucial guidelines must always be kept in mind when attempting to implement this system:

- Each step of the PSP fabrication process must be thoroughly controlled and validated to obtain satisfactory results and replicability. As with any silicon manufacturing process, good manufacturing practice is the key to a high-throughput, high-yield process producing functional devices according to specifications.
- The surface modification process of the PSPs can lead to a significant loss of PSPs during the several steps required. To minimize this loss, it is highly recommended that a small amount of detergent (i.e., Triton X-100) is added to pellet down the PSPs. In a volume of 300–600 μL , 1–2 μL of Triton can help recovering millions of

PSPs that may have otherwise been discarded with the supernatant. However, at the user's earliest convenience, this detergent should be removed from the surface of the PSP since it may inhibit the further modifications required.

- The loading and release kinetics of second-stage NPs can be controlled by tailoring the first-stage PSP's features. Confocal microscopy can be used to confirm optimal loading conditions, determine the distribution of multiple second-stage NPs, and ensure homogeneity within each first-stage PSP analyzed.
- Procedures described include using flow cytometry to determine shape, size, and intensity, Z2 Coulter Counter to analyze the concentration and size distribution, and ICP-AES to quantify the amount of silicon in solution. These methods provide details regarding the status of the PSPs and therefore need to be calibrated using control samples of known and defined nature prior to each analysis.

The quantification of trace amounts of silicon must be performed meticulously to obtain an accurate quantification. When preparing samples, it is essential that no tool/material comes into contact with glass. In the construction of the standard curve, the selection of the correct concentrations (standards have to adequately represent the range of expected values) greatly increases the accuracy of the measurements.

After successfully replicating the methods outlined earlier, the reader can modify and expand them in order to better suit its specific application. The versatility of the MDS technology allows users to easily build upon the core methods and to adapt them to a variety of different drug delivery scenarios. In particular:

- The design of the PSP size and shape can be optimized to enhance the PSP function using proprietary mathematical algorithms developed in our laboratory [45, 46]. While other NPs follow the laminar flow through the center of the capillary, the PSP tumbles along the wall of the capillary and eventually binds to markers on the tumor associated endothelial capillary wall.
- The PSPs can be surface modified with peptide sequences used to target tumor cells incorporated into the tumor vasculature. The PSP can use humanized monoclonal antibodies or peptide sequences and specific aptamers in order to avoid antibody targeting limitations and increase system stability.
- The possibility to maximize drug/second-stage NP loading and release through the modulation of PSP external and internal surface charges.
- Controlling the details of the pore structure, the PSP can be engineered to deliver drug or secondary NPs only in the direction of the endothelium. This minimizes the amount of NPs swept away in the bloodstream immediately after their release. It is also possible to obtain a PSP where only the external corona is functionalized with targeting moieties, the nucleation layer has been removed, and a small pore layer has been formed on the opposite side of the PSP. Such a PSP will attach to the endothelium with the nucleation layer facing the endothelial cells, and the release of NPs will occur only in one direction: from the nucleation layer towards the vessel wall.
- PSPs can be engineered to deliver drug and/or second-stage NPs upon endothelial binding or at a tuned delivery rate. Enzymatically degradable cross-linking peptides or pH-responsive polymers could be dispersed within the porous matrix of the PSP alongside NPs for environmentally triggered release.

- Functionalization with permeation enhancers will enable the PSPs to open tight junctions of the endothelial lining, through which NPs can pass to augment and/or create appropriate EPR conditions.
- The MDS is capable of codelivering drug cocktails. Many chemotherapy protocols involve a combination of drugs given together or in sequence. The PSP payload volume is large enough to carry a cocktail of free drugs and/or drugs containing NPs, together with thermal ablation agents and imaging NPs.
- The MDS enables In Silico Delivery Design to create a personalized therapy for each drug/disease combination. As the pharmaceutical industry has utilized large combinatorial compound libraries to identify new drug candidates, similarly, the MDS can be assembled in a combinatorial way optimizing shape, size, chemistry, surface targeting modalities, and charge modifications of the PSP, for the wide choice of available NPs.

Troubleshooting Table

Problem	Explanation	Potential Solutions
Si ₃ N ₄ film is not uniform.	Nonuniform gas distribution during LPCVD. Nonuniform temperature during LPCVD.	Add more dummy wafers. Move the relative position of the substrate to the gas source. Flip the substrate facing the direction with respect to the gas source. Change the position of the substrate within LPCVD tube. Wait longer for temperature stabilization before gas insertion. Improve temperature uniformity in the tube tuning the Si ₃ N ₄ deposition recipe.
Litographic pattern is: 1) too small or absent. 2) too large or photoresist is absent. 3) nonuniform.	The pattern is: 1) underexposed or under-developed. 2) overexposed or overdeveloped. 3) improperly exposed or developed. OR The mask or substrate is contaminated with dust.	1) Increase exposure or development time. 2) Decrease exposure or development time. 3) Vary exposure or development time. OR Clean the mask/substrate: acetone-methanol-isopropanol or piranha.
PSP is: 1) too flat. 2) too rounded. 3) too thin. 4) too thick. 5) cracked. 6) is not released. 7) released ahead of time.	1) Dry etch is too shallow. 2) Dry etch is too deep. 3) Porosification time is too short. 4) Porosification time is too long. 5) Porosification or release current density is too high. 6) Release current density is too low. 7) Release current density is too high.	1) Increase dry etch time. 2) Decrease dry etch time. 3) Increase porosification time. 4) Decrease porosification time. 5) Reduce release current density or porosification current density. 6) Increase release current density. 7) Reduce release current density.
Pore size is: 1) too big. 2) too small.	Porosification current density is: 1) too high. 2) too low.	1) Reduce porosification current density. 2) Increase porosification current density.
ZZ's aperture is blocked.	Dirty cuvette or ISOTON.	Hit "UNBLOCK" on control panel; OR Remove sample, wash aperture, load Accuvette with filtered ISOTON, hit "FUNCTION" → "FLUSH APERTURE"

Problem	Explanation	Potential Solutions
Z2's software shows more than one central peak [Figure 13.11(b)].	Small second peak: Large number of PSPs sticking together; OR Large second (or more) peak(s): PSPs breaking up within sample being measured (seen with PSPs with high porosity).	Briefly sonicate the sample longer. Check sonicator water level; the water needs to be set at the marked operating level.
"RUN" button on FACSCalibur is not green after pushed or the Status is Standby.	The machine cannot build up enough pressure to create the proper flow rate to introduce PSPs into the system.	If tube does not fit properly and you hear pressure/gas leaving the top of tube, try a new tube or replace the o-ring.
FACSCalibur's software shows a high noise or background acquisition.	The sensitivity of the machine is set such that it can detect extremely small particles/events, which inherently results in the detection of any dust or dirt that may be present in the system due to previous samples or poor cleaning.	Allow the machine to aspirate distilled water, and measure the tube with water and observe the number of events; if large, repeat. If after several cycles of aspirating water does not work, check sheath fluid level and replenish if necessary.

Acknowledgments

The authors would like to recognize M. Landry for excellent graphical support, Dr. D.L. Haviland for his superior expertise and experience with flow cytometry, Dr. Glen Snyder for his technical support at ICP-AES, Dr. Kaushal Rege for his continual support and useful commentary when compiling this chapter, and all present and past members of The Division of NanoMedicine for useful discussion and assistance.

References

- [1] Pope-Harman, A., et al., "Biomedical nanotechnology for cancer," *The Medical Clinics of North America*, Vol. 91, No. 5, September 2007, pp. 899–927.
- [2] Moghimi, S.M., A.C. Hunter, and J.C. Murray, "Nanomedicine: current status and future prospects," *FASEB Journal*, Vol. 19, 2005, pp. 311–330.
- [3] Debbage, P., "Targeted drugs and nanomedicine: present and future," *Curr. Pharm. Des.*, Vol. 15, No. 2, 2009, pp. 153–172.
- [4] Northfelt, D.W., et al., "Doxorubicin encapsulated in liposomes containing surface-bound polyethylene glycol: pharmacokinetics, tumor localization, and safety in patients with AIDS-related Kaposi's sarcoma," *J. Clin. Pharmacol.*, Vol. 36, No. 1, 1996, pp. 55–63.
- [5] Decuzzi, P., et al., "The effective dispersion of nanovectors within the tumor microvasculature," *Ann. Biomed. Eng.*, Vol. 34, No. 4, 2006, pp. 633–641.
- [6] Müller, R.H., et al., "Phagocytic uptake and cytotoxicity of solid lipid nanoparticles (SLN) sterically stabilized with poloxamine 908 and poloxamer 407," *J. Drug Target.*, Vol. 4, No. 3, 1996, pp. 161–170.
- [7] Ten Tije, A.J., et al., "Pharmacological effects of formulation vehicles : implications for cancer chemotherapy," *Clin. Pharmacokinet.*, Vol. 42, No. 7, 2003, pp. 665–685.
- [8] Katragadda, S., et al., "Role of efflux pumps and metabolising enzymes in drug delivery," *Expert Opin. Drug Deliv.*, Vol. 2, No. 4, 2005, pp. 683–705.
- [9] Bassingthwaighe, J.B., C.Y. Wang, and I.S. Chan, "Blood-tissue exchange via transport and transformation by capillary endothelial cells," *Circ. Res.*, Vol. 65, 1989, pp. 997–1020.
- [10] Silva, G.A., "Nanotechnology approaches to crossing the blood-brain barrier and drug delivery to the CNS," *BMC. Neurosci.*, Vol. 9, 2008, pp. Suppl 3:S4.
- [11] Jang, S.H., et al., "Drug delivery and transport to solid tumors," *Pharm. Res.*, Vol. 20, No. 9, 2003, pp. 1337–1350.
- [12] Jain, R.K., "Transport of molecules, particles, and cells in solid tumors," *Annu. Rev. Biomed. Eng.*, Vol. 1, 1999, pp. 241–263.

- [13] Nies, A.T., "The role of membrane transporters in drug delivery to brain tumors," *Cancer Letters*, Vol. 254, 2007, pp. 11–29.
- [14] Sakamoto, J., et al., "Antibiological barrier nanovector technology for cancer applications," *Expert Opin. Drug Deliv.*, Vol. 4, 2007, pp. 359–369.
- [15] Peer, D., et al., "Nanocarriers as an emerging platform for cancer therapy," *Nat. Nanotechnol.*, Vol. 2, No. 12, 2007, pp. 751–760.
- [16] Gabizon, A.A., "Stealth liposomes and tumor targeting: one step further in the quest for the magic bullet," *Clin. Cancer Res.*, Vol. 7, No. 2, 2001, pp. 223–225.
- [17] Decuzzi, P., et al., "Intravascular delivery of particulate systems: does geometry really matter?" *Pharm. Res.*, Vol. 26, No. 1, 2009, pp. 235–243.
- [18] Eckelman, W.C., and C.A. Mathis, "Targeting proteins in vivo: in vitro guidelines," *Nucl. Med. Biol.*, Vol. 33, No. 2, 2006, pp. 161–164.
- [19] Brannon-Peppas, L., and J.O. Blanchette, "Nanoparticle and targeted systems for cancer therapy," *Adv. Drug Deliv. Rev.*, Vol. 56, 2004, pp. 1649–1659.
- [20] Yezhelyev, M.V., et al., "Emerging use of nanoparticles in diagnosis and treatment of breast cancer," *Lancet Oncol.*, Vol. 7, 2006, pp. 657–667.
- [21] Lin, M.Z., M.A. Teitell, and G.J. Schiller, "The evolution of antibodies into versatile tumor-targeting agents," *Clin. Cancer Res.*, Vol. 11, 2005, pp. 129–138.
- [22] Farokhzad, O.C., J.M. Karp, and R. Langer, "Nanoparticle-aptamer bioconjugates for cancer targeting," *Expert Opin. Drug Deliv.*, Vol. 3, No. 3, 2006, pp. 311–324.
- [23] Simberg, D., et al., "Biomimetic amplification of nanoparticle homing to tumors," *Proc. Natl. Acad. Sci. USA*, Vol. 104, No. 3, 2007, pp. 932–936.
- [24] Yang, X., et al., "Selection of thioaptamers for diagnostics and therapeutics," *Ann. N. Y. Acad. Sci.*, Vol. 1082, 2006, pp. 116–119.
- [25] Allen, T.M., "Ligand-targeted therapeutics in anticancer therapy," *Nat. Rev. Cancer*, Vol. 2, No. 10, 2002, pp. 750–763.
- [26] Duncan, R., "Designing polymer conjugates as lysosomotropic nanomedicines," *Biochem. Soc. Trans.*, Vol. 35, Pt. 1, 2007, pp. 56–60.
- [27] Ferrari, M., "Nanovector therapeutics," *Curr. Opin. Chem. Biol.*, Vol. 9, No. 4, 2005, pp. 343–346.
- [28] Ferrari, M., "Cancer nanotechnology: opportunities and challenges," *Nature Rev. Cancer*, Vol. 5, No. 3, 2005, pp. 161–171.
- [29] Tasciotti, E., et al., "Mesoporous silicon particles as a multistage delivery system for imaging and therapeutic applications," *Nat. Nanotechnol.*, Vol. 3, No. 3, 2008, pp. 151–157.
- [30] Canham, L.T., et al., "Derivatized mesoporous silicon with dramatically improved stability in simulated human blood plasma," *Adv. Mater.*, Vol. 11, No. 18, 1999, pp. 1505–1507.
- [31] Cohen, M.H., et al., "Microfabrication of silicon-based nanoporous particulates for medical applications," *Biomedical Microdevices*, Vol. 5, No. 3, 2003, pp. 253–259.
- [32] Serda, R.E., et al., "Porous silicon particles for imaging and therapy of cancer," *Nanomaterials for the Life Sciences*, 2009.
- [33] Canham, L.T., *Properties of Porous Silicon: Crystal Research and Technology*, Vol. 34, New York: Wiley-VCH, 1999.
- [34] Decuzzi, P., et al., "Adhesion of microfabricated particles on vascular endothelium: a parametric analysis," *Ann. Biomed. Eng.*, Vol. 32, 2004, pp. 793–802.
- [35] Zhang, M., T. Desai, and M. Ferrari, "Proteins and cells on PEG immobilized silicon surfaces," *Biomaterials*, Vol. 19, No. 10, 1998, pp. 953–960.
- [36] Nashat, A.H., M. Moronne, and M. Ferrari, "Detection of functional groups and antibodies on microfabricated surfaces by confocal microscopy," *Biotechnol. Bioeng.*, Vol. 60, No. 2, 1998, pp. 137–146.
- [37] Nijdam, A.J., et al., "Physicochemically modified silicon as a substrate for protein microarrays," *Biomaterials*, Vol. 28, No. 3, 2007, pp. 550–8.
- [38] Anglin, E.J., et al., "Porous silicon in drug delivery devices and materials," *Adv. Drug Deliv. Rev.*, Vol. 60, 2008, pp. 1266–1277.
- [39] Akin, D., et al., "Bacteria-mediated delivery of nanoparticles and cargo into cells," *Nature Nanotechnology*, Vol. 2, No. 7, 2007, pp. 441–449.
- [40] Xiang, L., et al., "Bacterial magnetic particles (BMPs)+PEI as a novel and efficient non-viral gene delivery system," *The Journal of Gene Medicine*, Vol. 9, 2007, pp. 679–690.
- [41] Steinfeld, U., et al., "T lymphocytes as potential therapeutic drug carrier for cancer treatment," *Intl. Jour. of Pharm.*, Vol. 311, 2006, pp. 229–236.
- [42] Souza, G.R., et al., "Networks of gold nanoparticles and bacteriophage as biological sensors and cell-targeting agents," *Proc. Natl. Acad. Sci. USA*, Vol. 103, No. 5, 2006, pp. 1215–1220.
- [43] "Z2 COULTER COUNTER Cell and Particle Counter," Beckman Coulter, http://www.beckman.com/products/instrument/partChar/pc_z2.asp, last accessed on February 2, 2009.

- [44] Rahil-Khazen, R., et al., "Validation of inductively coupled plasma atomic emission spectrometry technique (ICP-AES) for multi-element analysis of trace elements in human serum," *Scand. J. Clin. Lab. Invest.*, Vol. 60, No. 8, 2000, pp. 677–686.
- [45] Gentile, F., et al., "The effect of shape on the margination dynamics of non-neutrally buoyant particles in two-dimensional shear flows," *Jour. of Biomech.*, Vol. 41, 2008, pp. 2312–2318.
- [46] Decuzzi, P., et al., "A theoretical model for the margination of particles within blood vessels," *Ann. Biomed. Eng.*, Vol. 33, No. 2, 2005, pp. 179–190.

Mathematical Modeling of Nanoparticle Targeting

Elena V. Rosca^{1,2} and Michael R. Caplan^{1,2*}

¹Harrington Department of Bioengineering, Arizona State University, ²Center for Interventional Biomaterials, Arizona State University

*Corresponding Author: Michael R. Caplan, Harrington Department of Bioengineering, Arizona State University, P.O. Box 879709, Tempe, AZ 85287-9709, Phone: 480-965-5144, Fax: 480-727-7624, e-mail: Michael.Caplan@asu.edu.

Abstract

Mathematical models based on the principle of conservation of mass can greatly enhance understanding of the behavior of and lead to design principles for nanoparticles used for drug or image contrast agent targeting. Implementing such models can be performed at the molecular scale, tissue scale, and organism scale, or at combinations of these scales. Molecular scale modeling is focused on changes in concentrations of bound and unbound nanoparticles with respect to time using chemical kinetics. Tissue scale modeling adds convection and diffusion within tissues along with reaction terms as in molecular scale modeling. Organism scale modeling uses compartmental models with rates of mass exchange between compartments. Once the model is capable of generating accurate predictions of the system's behavior under conditions not yet studied, the equations on which the model is based most likely incorporate the physical phenomena important to the behavior of the nanoparticles.

Key terms

mathematical modeling
nanoparticles
drug delivery
mass transport
protein binding
ligands
cell surface receptors

14.1 Introduction

All branches of science and engineering rely on some type of modeling to analyze, interpret, or explain data. Therefore, models serve diverse functions from aiding scientists in organizing data to deciding what data mean and developing an understanding of complex phenomena [1]. For example, understanding a complex event from empirical experimentation might prove to be a difficult and daunting task involving multiple trials to uncover the complex interplay of the principles involved. A theoretical model cannot only be helpful but sometimes critical to understanding the complex interplay of important factors affecting a system's behavior. Mathematical models are a class of models that involve the use of mathematics to describe a set of physical phenomena quantitatively. Such models allow a researcher to simulate one possible set of relationships among the components that he or she deems important. Comparison of the simulation results to experimental data can indicate that the factors that the scientist deemed important are indeed working the way modeled if the model and data produce similar results. If a large disparity between predicted and experimental data is observed, the model is perhaps too simplistic (omitting major underlying phenomena) or the interactions may be modeled incorrectly. If the discrepancy is relatively small, perhaps some parameters are estimated inaccurately.

This can be thought of as using a model as a hypothesis generator. The model is in fact a statement of the hypothesis: that the physical components of the system relate as described in the mathematics. The model is then used to simulate what would happen under various sets of conditions to find a set of theoretical results that, if found to exist in reality, would lend credence to the relationships being as they are described in the model. The experiments are then performed, and the experimental results are compared to the theoretical predictions as described above. If there is a good fit between prediction and data, it is possible that the phenomena are accurately described in the model. However, the normal caveats about experimental validation of hypotheses apply, namely, that one test of a hypothesis does not prove the hypothesis to be true. Additionally, as we will discuss later in this chapter, there is the added caveat that a large number of fitted parameters can make a model fit many sets of data even if the model is not an accurate description of the physical phenomena.

Targeting with nanoparticles is a complex problem that encompasses multiple phenomena: interaction of the particle with the target cells, delivery throughout the tissue of interest, stability of targeting moieties (ligands), clearance by various organs, and others. Modeling these factors can assist in the rational development of more effective targeting particles. In particular, modeling can help researchers deal with tradeoffs inherent to the design process such as those between dose of particles and specificity [2]. Here we describe methods for modeling at three different length scales: (1) interactions of the particles with the target at the *molecular/cellular scale*, (2) delivery and diffusion/convection through tissue at the *tissue scale*, and (3) systemic delivery, clearance, and biodistribution at the *organism scale*. At each of these scales, this chapter discusses the available modeling techniques applicable to that length scale, provides in-depth discussion of how to apply those techniques, and indicates how these techniques can be or have been applied to advance targeting of nanoparticles.

Molecular/cellular scale modeling is mainly concerned with interaction between the nanoparticles and cell surface receptors. Typically nanoparticles are carriers of specific molecules (ligands) able to interact with cell surface receptors effectively creating

multivalent constructs [3–8]. Modeling at this level has been focused on understanding the effects of multivalent interactions. These studies suggest that multivalent interactions exhibit increased avidity (overall increased binding of the constructs of higher valency), which is predicted to result in greater targeting specificity [2]. Chemical kinetics are used to describe the interactions between such multivalent particles and cells. Thermodynamics can be used to better estimate parameters for these biophysical models [8, 9].

Tissue scale modeling adds diffusion and/or convection of the particles through the tissue in which the target cells reside. One method of delivery to tumor can be via passive transport from the blood due to high permeability and multiple fenestrations in tumor vasculature [10–12]. Mass transport in these cases is a function of diffusion, interstitial pressure, and tumor pressure. Tissue heterogeneity and anisotropy are also factors that affect fluid distribution. A different approach to delivery consists of local delivery followed by diffusion and/or perfusion [13, 14]. Models in this case are concerned with bulk fluid flow velocities, tissue permeability, filtration of nanoparticles, and other parameters that can influence nanoparticle distribution within the tissue.

Last, modeling at the organism scale involves a much broader view of the issue at hand. This scale typically seeks to address biostability, biodistribution, and clearance rates of the nanoparticles. Some parameters important in organism scale modeling are the size of the particles, injection volume and location, dose frequency, and concentration [15]. Such issues are often studied using compartmental models in which the organs or tissues encountered by the particle are modeled as compartments that are interconnected through rates of transfer from one compartment to another.

14.2 Molecular/Cellular Scale

14.2.1 Methods

In molecular/cellular scale modeling of nanoparticles, the model describes binding of the particle with the target cell via the cells' surface receptors or other surface-bound markers. The most widely used method to study biophysics at this scale is chemical kinetics. Also known as receptor-ligand modeling, this approach was first adapted to study binding of molecules to cell surface receptors by Perleson [16] and has since been extensively reviewed by Lauffenburger and Linderman [17]. The foundation for this type of model is a single binding event between a cell surface receptor and a soluble ligand (such as a growth factor) forming a bound complex. This event can be described and simulated mathematically using the principle of conservation of mass with the following set of equations:

$$\frac{dL}{dt} = -k_f LR + k_r C \quad (14.1)$$

$$\frac{dC}{dt} = k_f RL - k_r C \quad (14.2)$$

$$R = R_0 - C \quad (14.3)$$

where L is the concentration of the ligand, R is the concentration of the unbound receptor, C is the concentration of the receptor-ligand complex, k_f is the association rate, k_r is the dissociation rate, and R_0 is the total density of receptors. Equations such as these can be written using the following procedure:

1. Determine the number of terms in each equation. Equations (14.1) and (14.2) have two terms each because each species (L for (14.1) and C for (14.2)) participates in two reactions (association $L + R \rightarrow C$ and dissociation $C \rightarrow L + R$).
2. Determine the species variables (concentrations) that must be in each term. The reactants always determine kinetic order (note: these must be mechanistic reactions, not overall stoichiometry). The first term, describing association, is written with second-order kinetics since two freely moving molecules must collide for association to occur. The second term, describing dissociation, is written with first-order kinetics because only the presence of receptor-ligand complexes (no collision) is necessary for these events to occur. The appropriate rate constant is then added to each term.
3. Determine the sign of each term. The signs of each term are written to describe whether association or dissociation adds (+) or removes (–) ligand or complexes from the system. It can be seen by adding (14.1) and (14.2) that the overall change in mass of the system with time is zero; thus, mass is conserved. Mass must be conserved for the overall system.

These equations are inserted into a program which can solve ordinary differential equations such as MATLAB (Mathworks) as follows:

1. Enter each parameter value by naming them *p.name* with the syntax “p.kf = 1e6;” for the example of setting the association rate to 1×10^6 . Also enter initial conditions and the time at which the simulation will end (p.tf) using the same syntax. Note that the user must make sure units (e.g., meters, seconds, and so forth) are consistent.
2. Enter “[t y] = ode15s(@equationfile, [0 p.tf], y0, options, p);” where “ode15s” is the ordinary differential equation solver chosen, “equationfile” is the name of the function where the equations are defined, “y0” is a row vector containing the initial conditions, options are defined as in MATLAB help, and “p” calls the parameter values defined above.
3. Output variables can be calculated. For example the number of unbound receptors could be calculated by “R = p.R0 – y(:,2);” where “y(:,2)” denotes y values in the second column of the [t y] matrix as a function of time. Figures can be plotted based on these calculated values or on the raw data as desired.
4. The equations are defined in a file beginning with “function yp = equationfile (t, y, p);” where “equationfile” must match the name supplied in step 2 exactly. The variables are defined as “L=y(1);” and “C=y(2)”. Immediately after this, any variables calculated with algebraic equations should be calculated, in this case $R(t)$ is defined as “R = p.R0 – C;”.
5. Finally the ordinary differential equations are defined as “yp(1) = -p.kf * L * R + p.k2 * C;” and “yp(2) = p.kf * L * R – p.kr * C;”.

Perleson and DiLisi extended this model by applying it to receptor clustering and binding of multivalent ligands (such as antibodies) to oligomeric receptors of B cells [16]. Since nanoparticles have many ligands bound to their surfaces, they likely behave similarly to these multivalent molecules. Converting Perleson and DiLisi’s model into

the notation used in this chapter, L_0 represents the total concentration of divalent molecules, C_1 represents the concentration of divalent molecules bound by one ligand to the cell, and C_2 represents the concentration of divalent molecules bound to the cell by two ligands, which also corresponds to the concentration of cross-links.

$$\frac{dL}{dt} = -2k_f R(t)L(t) + k_r C_1(t) \quad (14.4)$$

$$\frac{dC_1}{dt} = 2k_f R(t)L(t) - k_r C_1(t) - k_x C_1(t)R(t) + 2k_{-x} C_2(t) \quad (14.5)$$

$$\frac{dC_2}{dt} = k_x C_1(t)R(t) - 2k_{-x} C_2(t) \quad (14.6)$$

$$R_0 = R(t) + C_1(t) + C_2(t) \quad (14.7)$$

where k_x and k_{-x} are the association and dissociation rate constants of the second ligand to bind (thus forming the crosslink). These equations are generated in the same manner as described for the single ligand, but the coefficient 2 is necessary in (14.4) and (14.5) to adjust the probability of collision since there are two ligands on the divalent molecule and in (14.5) and (14.6) because a C_2 species occupies two receptors either of which can dissociate.

The rate constants, k_x and k_{-x} , differ from k_f and k_r by a factor accounting for the increased effective concentration of the ligand when it is tethered to the cell surface by the first receptor-ligand bond. Shewmake et al. [18] defined a factor, V_R , which accounts for the increased effective concentration. This *binding enhancement factor* corrects the association rate constant of secondary binding events in relation to the first binding event. Shewmake's work is based on work by Krishnamurthy, Whitesides, and coworkers [8], who modeled an inhibitor tethered to the enzyme which it inhibits. Their model calculates C_{eff} which is similar to $V_R^* C_1$ in (14.11), as a function of the root-mean-squared distance between the ends of the polymeric linker, $R_g = \langle r^2 \rangle^{1/2}$, and the distance between tether site and binding site, a . Shewmake et al. applied this to multivalent targeting for several cases, including a random-coil model for linkers between ligands resulting in:

$$V_R = \varphi I h \quad (14.8)$$

$$I = \frac{(3)^{1/2}}{(2\pi)^{1/2} R_g} \exp\left(-\frac{3a^2}{2R_g^2}\right) \quad (14.9)$$

where φ is a scalar accounting for excluded volume and h is the ratio of interstitial fluid and the cell surface area.

Caplan and Rosca applied this model to multivalent targeting by allowing for two or more different cell types that differ only in the number of receptors expressed (cell types with different R_0 values). Using this model they investigated the binding of targeting molecules with various valence (monovalent, divalent, trivalent, and tetravalent), of which various concentrations were applied to cells, and for constructs targeting one receptor type (homovalent) or two receptor types (heterovalent). For the homo,bivalent

model, (14.4) is modified to allow binding of the unbound construct to two different cell types, M and N :

$$\frac{dL}{dt} = k_r(C_{1M} + C_{1N}) - 2k_f(R_M + R_N) \quad (14.10)$$

Two sets of (14.5) to (14.7) are created, one set for constructs bound to cell type M and another set for constructs bound to cell type N . An additional difference from (14.4) to (14.7) is the introduction of the parameter V_R , the binding enhancement factor. The introduction of this parameter allows the replacement of k_x and k_{-x} with k_f and k_r , because V_R encompasses the effects of secondary binding events of the multivalent constructs so, for instance, the equation for C_{1M} (C_1 binding to cell type M) becomes:

$$\frac{dC_{1M}}{dt} = 2k_fLR_M - k_rC_{1M} - k_fV_R C_{1M}R_M + k_rC_{2,M} \quad (14.11)$$

in which the association rate between C_{1M} and an additional receptor is multiplied by V_R .

This model can be used to test the dominant premise of targeting, that more drug or imaging molecules will be bound to the target cell, by taking the ratio of constructs bound to the target cell ($C_{1M} + C_{2,M}$) versus the number of constructs bound to nontarget cells ($C_{1,N} + C_{2,N}$). This ratio, defined as *specificity*, provides a quantitative description of how effective the targeting would be under such conditions.

14.2.2 Data Acquisition, Anticipated Results, and Interpretation

The equations in and of themselves are the mathematical representation of the physical phenomena, but most often they are a means to an end rather than the ultimate goal. In this case, Caplan and Rosca sought to use the mathematical model to elucidate principles for rational design of such multivalent constructs. By considering the possible ways in which the constructs could be designed or employed, several points of control became apparent by which designers can modify constructs. In this system these include the affinity of the receptor-ligand bond, the number of receptors on the target cell, the ratio of the receptors between target and nontarget cells, the concentration of the construct (dose), number of ligands on the construct (valence), and the properties of the linker between ligands. These correspond to parameters in the equations or initial conditions K_D (k_r/k_f), $R_{0,M}$, $R_{0,M}/R_{0,N}$, L_0 , n (as in C_n), and V_R respectively.

Caplan and Rosca varied the receptor number on the target cell ($R_{0,M}$), construct concentration (L_0), and valence (n) while keeping the other parameters constant. They developed sets of equations for homo,trivalent, homo,tetravalent, hetero,divalent (two ligands of each type), and hetero,trivalent (three ligands of each type) constructs similar to those shown above. Results from these models, shown in Figure 14.1, depict the simulated binding specificities of multivalent constructs when the initial construct concentration (Figure 14.1(a)) and the number of receptors on the target cells (Figure 14.1(b)) are varied.

14.2.3 Discussion and Commentary

Illustrating the purpose of modeling at this scale, it is instructive to note several things. First, Caplan and Rosca were able to narrow the scope of their experimental study from

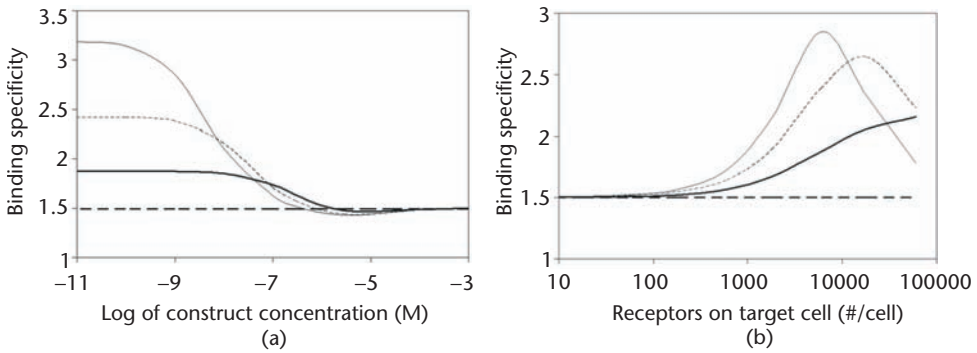


Figure 14.1 Binding specificity of different constructs (monovalent is depicted by a thick dashed line, divalent is depicted by a thick solid line, trivalent is depicted by a thin dashed line, and tetraivalent is depicted by a thin solid line) as (a) construct concentration and (b) receptor numbers are varied. (From: [2]. © 2005 Reproduced with permission from Elsevier.)

all possible variations in the design of these constructs to those aspects of the design that had direct correlations to parameters in the mathematical equations. Likewise, the need to quantify a measure of output, in this case specificity, highlighted the need to study binding to two different cell types. In vitro characterization of targeted constructs pre-dating this work studied binding of constructs to the target cell type and control experiments were typically constructs with a nonfunctional ligand. Modeling showed that multivalency could achieve increased *avidity* for the target cell type without necessarily increasing *specificity* for the target cell type. Thus, merely writing the equations and choosing how to quantify the output of the model provided an advance to the field in the form of clarifying this metric.

Second, the model yielded insights that would not be available by intuition alone or, if intuition could have achieved them, were not intuited prior to the application of this model. Modeling provides a formalism for breaking very complex problems down into manageable pieces which can then be assembled into the mathematical models described. The molecular scale models shown here are broken down into equations for each species of interest (e.g., L , C_1 , C_2 , and so forth), and each of these equations is further broken down into a summation of terms which each represent an association or dissociation event. When these pieces were reassembled and parameters varied, the results produced provided insights that were not initially obvious.

For example, when the concentration of construct was varied (Figure 14.1(a)), the specificities of multivalent constructs at high concentration were no different than those for monovalent. At low concentration, however, the expected trend for which specificity increases as valence increases was predicted. Since the model keeps track of the various individual species (C_1 , C_2 , and so forth), Caplan and Rosca were able to determine that this was due to the prevalence of C_1 species at high concentration, which in effect made all binding monovalent due to saturation of the available receptors even when the constructs were multivalent. In a similar manner, when receptor density on the target cell was varied, a biphasic trend was observed with specificity increasing at lower receptor number and decreasing at higher receptor number. Again, availability of information on the individual species revealed that specificity is mostly a function of the percentage of constructs bound by most or all of the ligands (C_2 for divalent, C_3 for trivalent, and so forth). At lower receptor numbers, the percentage of these species

increases more rapidly on target cells than on nontarget cells; however, at higher receptor numbers, the percentage on target cells approaches 100%, so the percentage increases more rapidly on nontarget cells. Thus, although the avidity monotonically increases with increasing receptor numbers, specificity is predicted to be biphasic.

These insights provide general design principles that can be used to increase the likelihood of successful application of nanoparticle targeting. The results shown in Figure 14.1 indicate that the receptor-ligand binding affinity should be two to three orders of magnitude weaker than the required dose if multivalency is to achieve specificity in excess of the ratio of receptors. Additionally, a receptor target which expresses a mid-range number of receptors must be chosen even though a receptor at very low or very high copy number might have a greater ratio of expression between target and nontarget. Experiments must then be performed to validate such design principles, but modeling can provide the initial impetus to perform such experiments and indicate how one should carry out the experiment to see the predicted result.

14.3 Tissue Scale

14.3.1 Methods

Tissue scale modeling can be used to address spatial variations in tissues. An example of this level of modeling is diffusion/convection modeling of nanoparticles delivered directly to tissue containing a tumor. Models at the tissue scale can also account for spatial variations in tissue or construct that arise either due to tissue architecture, such as the growth of a tumor in the tissue, or through delivery of the construct in a particular way (e.g., systemically through the blood or injected directly into the tissue). The application of the principle of conservation of mass to such convection/diffusion problems has a very long history, but recently these principles have been applied directly to nanoparticle targeting.

Morrison et al. [19] developed a model describing the injection of macromolecules into brain tissue in which the macromolecules can convect with fluid flow, diffuse, be driven across a capillary wall into the blood stream, or be inactivated by metabolism.

$$R_d \frac{\partial C}{\partial t} = D_e \nabla \cdot (\phi \nabla C) - \nabla \cdot (\phi v C) - \left[L_p s (1 - \sigma) (p_e - p_i) / (e^{P_{emv}} - 1) \right] C - k_{in} C \tag{14.12}$$

where R_d accounts for the distribution of the macromolecule between the intracellular and extracellular space, D_e is the effective diffusion coefficient, ϕ is the volume fraction not filled by cells or extracellular matrix, L_p is the vascular hydraulic conductivity, s is the capillary surface area per volume of tissue, p_i and p_e are the interstitial and Starling pressures, P_{emv} is the microvascular Peclet number, and k_{in} is the rate constant for degradation of the macromolecule. This equation accounts for accumulation of the biomacromolecule with time (left side), diffusion (first term, right), convection (second term, right), loss to the blood stream (third term, right), or deactivation (fourth term, right). Solving (14.12) requires one initial condition (in this case $C = 0$ at $t = 0$) and two boundary conditions. One boundary condition at the injection site ($r = 0$) is set so that the concentration of the macromolecule in the injection is held constant ($C = C_0$). A typical second boundary condition used as $r \rightarrow \infty$ is that the concentration remains

unchanged ($C = 0$ at $r = \infty$). Morrison et al. use a simplified version of this equation, in which the third term is omitted, to model convection-enhanced delivery to the brain of a therapeutic molecule which cannot cross the blood-brain barrier. Similar models can be applied to delivery of nanoparticles to tissue if parameter values are known for D_c and the retardation coefficient (σ) of the particles in the tissue. Rosca et al. [20] have best fit these values for targeted polymers and quantum dots and found that D_c values of 6×10^{-6} and 1×10^{-6} and filtration coefficients ($1 - \sigma$) of 1 and 0.25, respectively, describe the diffusion/convection of these particles in an agarose mock of brain tissue.

Stukel et al. [21] have incorporated the molecular scale binding interactions discussed above into Morrison et al.'s model of convection-enhanced delivery. In the study, brain tissue was modeled using a nodal network with a region of healthy cells and a subdomain of tumor cells. The method presented here is the finite difference scheme used by Stukel et al.; however, it is possible to perform similar modeling using COMSOL Multiphysics which is a finite element simulation. The method described for molecular scale modeling is modified as follows:

1. Equations are derived as in molecular scale modeling; however, there are additional terms for diffusion, $D\nabla^2 L$, and convection, $-v\nabla L$, which can be modeled in Cartesian coordinates with Taylor series expansions:

$$D\nabla^2 L = D \left[\frac{\partial^2 L}{\partial x^2} + \frac{\partial^2 L}{\partial y^2} \right] = D \left[\frac{L_{i+1} + L_{i-1} - 2L_i}{h^2} + \frac{L_{j+1} + L_{j-1} - 2L_j}{k^2} \right] \quad (14.13)$$

$$(1-\sigma)v\nabla L = (1-\sigma) \left[v_x \frac{\partial L}{\partial x} + v_y \frac{\partial L}{\partial y} \right] = (1-\sigma) \left[v_x \left(\frac{L_i - L_{i-1}}{h} \right) + v_y \left(\frac{L_j - L_{j-1}}{k} \right) \right] \quad (14.14)$$

where h and k are the distance between nodes in the x and y coordinates respectively, L_i is the construct concentration at x -position i , and L_j is the construct concentration at y -position j .

2. These equations are now nested in a loop structure which varies i and j from 1 to n and 1 to m , respectively, where nh and mk are the dimensions of the tissue. The tumor is defined as several i, j pairs and distinguished by a greater $p.R0$ value.
3. Boundary conditions are set at $i = 0$, $i = n + 1$, $j = 0$, and $j = m + 1$. Concentration boundary conditions are set as $L_{0,j} = 1e-9$, for the example of a constant concentration boundary condition at $i = 0$. No flux boundary conditions can be set by declaring $L_{0,j} = L_{1,j}$ since there will be no flux at this boundary because there can be no concentration gradient.

Stukel et al.'s model is intended to represent a catheter placed within brain tissue through which a solution of drug-targeting construct is injected and the fluid velocity is oriented radially outward from the source. Equations (14.15) and (14.16) describe the transport of drug-targeting constructs including convection. Equation (14.15) describes the equation in Cartesian coordinates, while (14.16) shows the equation in spherical coordinates for which the Cartesian equation is a 2-D simplification.

$$\frac{\partial \hat{L}}{\partial \hat{t}} = \left[\frac{\partial^2 \hat{L}}{\partial \hat{x}^2} + \frac{\partial^2 \hat{L}}{\partial \hat{y}^2} \right] - 3\alpha \hat{R} \hat{L} + \hat{C}_1 - \left[v_x \frac{\partial \hat{L}}{\partial \hat{x}} + v_y \frac{\partial \hat{L}}{\partial \hat{y}} \right] \quad (14.15)$$

$$\frac{\partial \hat{L}}{\partial t} = \frac{1}{\hat{r}^2} \frac{\partial}{\partial \hat{r}} \left(\hat{r}^2 \frac{\partial \hat{L}}{\partial \hat{r}} \right) - 3\alpha \hat{R} \hat{L} + \hat{C}_1 - \frac{\beta}{\hat{r}^2} \frac{\partial \hat{L}}{\partial \hat{r}} \quad (14.16)$$

where \hat{L} is the dimensionless concentration of unbound concentration (concentration scale is R_0), \hat{R} is the dimensionless unbound receptor density, \hat{C}_1 is the dimensionless density of complexes with one ligand bound, \hat{v}_x and \hat{v}_y are the dimensionless Cartesian components of $v_r = Q/4\pi r^2$ for which the flow rate, Q , is held constant at $3 \mu\text{L min}^{-1}$ ($\beta = (Q\sqrt{k_r})/(4\pi D^{3/2}) = 6,906.59$), and \hat{x} , \hat{y} , and \hat{r} are dimensionless coordinates ($\sqrt{D/k}$ is the length scale). α is a dimensionless parameter ($\alpha = R_0/K_D$) describing the relationship between receptor density and receptor-ligand affinity; β is a dimensionless parameter dependent on the radial velocity, from which the x and y velocity components, v_x and v_y , are calculated for each time and matrix location. The equations for C_1 , C_2 , C_3 , and R are calculated for each node at each time point, and these equations remain the same as in the model discussed in the molecular scale section. Boundary conditions are set at the catheter edge ($r = 0.64 \text{ cm}$) to be $\hat{L} = \hat{L}_{\text{injectate}}$ for $0 < t < t_c$, and $\hat{L} = 0$ for $t_c = t < t_f$ where t_c is 43,200 seconds. This simulates the injection of nanoparticles for some duration t_c and then injecting an artificial cerebrospinal fluid afterwards. The external boundary (edges far from catheter tip) is set to no-flux for all times. The source was placed in the center of the matrix. Initial condition for the tissue is $\hat{L} = 0$ at $t = 0$.

14.3.2 Data Acquisition, Anticipated Results, and Interpretation

Results from this diffusion/convection model of nanoparticle targeting are tracked as total constructs ($L + C_1 + C_2 + C_3$) at each node because imaging and/or therapy would depend on the total amount of construct—not just the amount bound to the cells. Figure 14.2 illustrates that enhancement of contrast occurs only when unbound construct is washed away from the tissue. Diffusion alone can accomplish this, but the time required is impractically long. This model predicts that convection-enhanced delivery can dramatically decrease the time required to achieve desirable levels of contrast between target and nontarget tissue. Figure 14.2 shows these results as well as demonstrates the volume of tissue that can be effectively probed using this approach.

14.3.3 Discussion and Commentary

The results from this diffusion/convection model reveal several points about nanoparticle targeting of cancer, particularly in the brain. First, even when tumor location is unknown, the model predicts that it is possible to achieve contrast in excess of 10:1 for tumor tissue versus surrounding tissue. Second, the time required for constructs to be convected to the tumor and then for unbound construct to be convected away from the tumor is large relative to typical imaging procedures but is reasonable for a clinical procedure. Combined with the third prediction, that concentration must be less than the receptor-ligand affinity to achieve high contrast, this severely limits the choice of contrast agents that can be used. Typical magnetic resonance imaging (MRI) contrast agents are long-lived but require high concentration. Conversely typical positron emission tomography (PET) contrast agents can be used at low concentration but are very short-lived (minutes). The convection-enhanced delivery model shown here quantifies

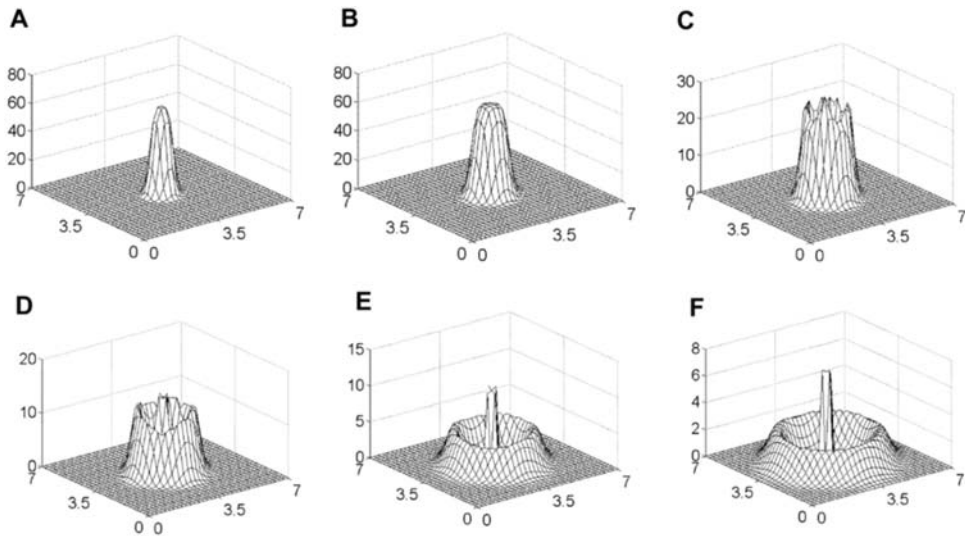


Figure 14.2 Concentration of targeting constructs achieved via convection-enhanced delivery at different time points and locations. Panels represent total construct concentration (z axis, molecules/cell) at each position (x and y axes, cm) at: (a) 12,000 seconds, (b) 43,000 seconds, (c) 86,000 seconds, (d) 172,000 seconds, (e) 432,000 seconds, and (f) 864,000 seconds. Contrast is visible at (d) $t = 172,000$ seconds and reaches maximum at (f) 864,000 seconds. (From: [21]. © 2008 Reprinted with permission from Elsevier.)

the problems of applying multivalent targeting to cancer imaging, but it also provides a means to study possible solutions to these issues.

14.4 Organism Scale

14.4.1 Methods

Models at the organism scale also make use of the principle of conservation of mass; however, using the approach discussed in the tissue scale modeling section would be impractical. This is due to several reasons including that the number of nodes required to accurately reflect whether tissue/organ architecture would be very large, architecture would require having regions in which diffusion dominates and regions in which convection dominates, and several other problems. Instead, when one needs to model nanoparticle targeting on the scale of the whole organism, compartmental models are typically used in which each compartment is modeled using one of the techniques discussed above and the connections between the compartments are typically modeled using mass transfer rates between compartments.

One recent example is the work of Davis et al., who investigated the efficacy of targeting and delivering siRNA to tumors using transferrin-targeted nanoparticles [22]. The model is comprised of three interconnected compartments: plasma, tumor interstitial volume, and tumor intracellular volume. Concentrations (mol/L) of siRNA in each of these spaces are defined as C_1 (plasma), C_2 (interstitial tumor), and C_3 (intracellular tumor). The equations governing the concentrations of the nanoparticles in these compartments are:

$$\frac{dC_1}{dt} = k_{21}C_2 \frac{V_2}{V_1} - (k_{12} + k_{elim})C_1 \tag{14.17}$$

$$\frac{dC_2}{dt} = k_{12}C_1 \frac{V_1}{V_2} + k_{32}C_3 \frac{V_3}{V_2} - (k_{21} + k_{23})C_2 \tag{14.18}$$

$$\frac{dC_3}{dt} = k_{23}C_2 \frac{V_2}{V_3} - k_{32}C_3 \tag{14.19}$$

These equations are derived similarly to the method described for molecular scale modeling with the difference that, instead of mechanistic reactions, the terms in each equation describe rates of transfer from one compartment to another and are typically written as first-order events. As can be seen in the schematic depiction of this model (Figure 14.3(a)), this is a relatively simple model in which the terms multiplied by k_{12} represent transfer from the blood to the tumor interstitial space, k_{21} the opposite, k_{23} represents uptake into tumor cells, k_{32} the opposite. The only additional term is the elimination of particles from the blood (k_{elim}). V_1 , V_2 , and V_3 are the volumes corresponding to each compartment, and the ratio of these volumes must be accounted for because the transfer between compartments is in mass per time; however, the variables being calculated are in concentration units.

14.4.2 Data Acquisition, Anticipated Results, and Interpretation

This model was validated against in vivo data by fitting the extravasation rate (k_{12}) and setting the rate of return to blood (k_{21}) and tumor uptake (k_{23}) to zero. As can be seen in Figure 14.3(b), the model result for nanoparticles in the tumor fits the experimental data very well if a dilution rate of 25 min^{-1} is included in the definition of total particles in the

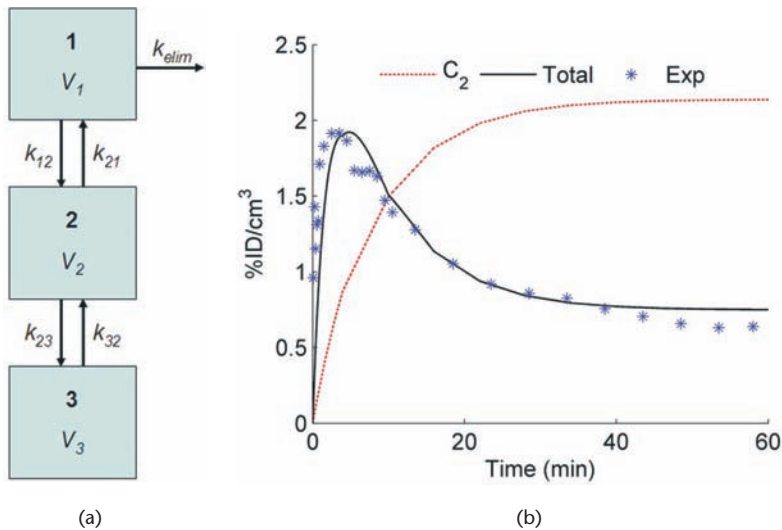


Figure 14.3 Compartmental modeling of tumor-specific targeting. (a) The three-compartment model that was used to derive the equations describing tumor targeting. (b) A comparison of model predictions to experimental data collected. (From: [22]. © 2007 Reprinted with permission from PNAS.)

tumor. It should be noted that the dilution effect would have been more accurately handled by adding convection terms in (14.17) accounting for particles being injected in (none in the dilutant, so this term is zero) and washed out ($-Q C_1/V_b$), where Q is the volumetric flow rate of the dilutant. If Q is set to a nonzero value for $t < 25$ minutes and to zero for $t > 25$ minutes, this would more accurately reflect the mass transport of the experiment performed by Davis et al.

14.4.3 Discussion and Commentary

The strength of organism scale modeling is that it gives a description of the behavior of the targeting construct within the overall study system, the organism. However, the limitation that is usually found in this type of model is the lack of mechanistic description of the physical meaning of the parameters. In this case, the model yields general information about the relative importance of the various transfer terms. For example, since the data can be fit by setting k_{21} and k_{23} to zero, we can reasonably conclude that uptake into the cells does not affect the concentration of particles in the tumor and that, once the particles enter the tumor, their rate of transfer back into the blood is negligible. We also see that the data can be fit reasonably well with a first-order rate of transfer from the blood to the tumor tissue. However, this sort of compartmental model does not provide any information as to why, mechanistically, the transfer from blood to tumor is first-order.

This limitation can potentially be overcome by combining a compartmental model with the molecular or tissue scale models discussed in the previous sections. For example, a model in which three compartments represent: (1) blood, (2) nontarget cells, and (3) tumor cells could be used. The rate of transfer from the blood to compartments 2 or 3 could be modeled using a term similar to the third term of the right side of (14.18) or using the terms representing binding of unbound constructs to cells as in (14.4). Once in either compartment 2 or 3, the equations describing the biophysics of multivalent interactions could track unbound (L) and the various bound constructs (C_1 , C_2 , and so forth). The only constructs which could be exchanged with the blood would be unbound constructs. Such a multiple-scale model could perhaps provide both the overall description of nanoparticle performance while also providing mechanistic detail that is necessary to use modeling as a design tool.

14.5 Model Validation and Application

14.5.1 Statistical Guidelines

Mathematical models of physiological systems or processes are approximations and estimations of the real system. The process of creating the model can generate error due to either under-parameterization or over-parameterization. An under-parameterized model, a too simplistic representation of the system, will give inaccurate predictions due to having made simplifying assumptions that are not quite true; thus, the predictions will be inaccurate if important phenomena were omitted due to such simplifications. An over-parameterized model, complex relative to the prior knowledge that the modeler has about the system, contains many parameters for which there is little to no prior information upon which to estimate those parameters. These parameters need to be fit

to data, and in many cases it is possible to fit experimental data even if the underlying equations are not accurate descriptions of the physical behavior of the system. This is probably the most common mistake because it is usually hidden under the impression that the equations provide a very good fit of the system's behavior [23]. To avoid the risk of over-parameterization, two general rules to follow are: (1) the number of data points should considerably exceed the number of parameters to be fitted, and (2) the technical behavior of the optimization process will improve as the ratio of data to parameters increases [24].

Fitting a model to data entails the adjustment of model parameters to achieve a concordance between the model prediction and the actual data. However, parameter estimation can be accomplished independently of fitting from previously existing data, and, if this estimated value is not adjusted in the fitting process, model validation is more meaningful [25]. Model fitting is often used to indicate the predictive value of the model; however, there is a clear distinction between the two. Model fitting takes a model that is missing several key parameter values and then trains the model by finding those parameter values that allow the model to best describe the data. As discussed earlier, if the model includes the phenomena important to the function of the system, it should be able to match the data closely. It is possible, particularly if the model is over-parameterized (fitting too many parameters), to match the data closely despite the fact that the model does not accurately describe the underlying phenomena. In such a case, if the model were to be used to predict what would happen if the conditions were changed and the experiment run again, it would predict poorly.

The procedure for best fitting parameters is as follows:

1. Create either a spreadsheet or a matrix with experimental data in one column and the model value for conditions identical to each experimental point in another column.
2. Subtract the model result from the data or vice versa.
3. Square the difference. This is the square of the error
4. Sum the "squares of the error."
5. Vary parameter values either manually or through an automated method (some software will have a feature that does this, but to do this in MATLAB requires writing a simple code to vary the parameters). Find the parameter set that minimizes the sum of squares of the error. These are the best-fit parameter values.

The true test of whether the model accurately reflects the phenomena important to the function of the system is to use the model to make a prediction under conditions not used to fit the parameters in the model. This process of predictive validation is closely related to hypothesis testing of an experimental hypothesis.

1. Use the model to make a prediction of what data will result under certain, previously unmeasured, conditions.
2. Perform experiments under those conditions to measure data. Perform sufficient replicates so that 95% confidence intervals are of reasonable size (this will depend on the level of accuracy desired in the model and variance in the experimental system).

- For each condition predicted/measured, compute the t-statistic between the average of the data (\bar{x}) and the model predicted value (x) using the equation $t = \frac{\bar{x} - x}{(\sigma/\sqrt{n})}$ where σ is the standard deviation of the data and n is the number of replicates.
- Compare the value of the t-statistic with the established t-value corresponding to the desired level of significance and degrees of freedom. If no statistical differences are found, the hypothesis that the model prediction was different from the data was not found to be valid, which is one indication that the model may be valid.

Determination of statistical significance by the method in step 3 is mathematically identical to plotting the experimental data with their confidence intervals (i.e., 95%, 99% confidence intervals) and the model prediction on the same plot and then visually inspecting to determine if the model predictions do or do not lie within the confidence intervals (this will only work with confidence intervals—not standard deviations or standard error of the mean). It is important to note that this approach will never reject the alternative hypothesis, and “not rejection” of the null hypothesis does not necessarily mean that the null hypothesis is true—only that there is not sufficient evidence against it. Also rejecting the null hypothesis does not mean that the alternative hypothesis is true—only that it is more accurate given the data. Similarly, with this approach one can never prove that the model is true—only that the conditions used to test the model did not demonstrate a flaw in the model.

Troubleshooting Table

Problem	Potential Solution
Code will not run.	Check syntax (i.e., parenthesis, operator, variable names). Function name/call do not match (also dashes or numbers in the name may cause this error).
Suspension on time steps.	Make equations dimensionless so that variables are on the same order of magnitude (~1). Try a different ordinary differential equation solver. Adjust tolerances.
Concentrations are negative.	Check equations. Check loop structure (for finite differences). Check for sign error in equations. Check order of reaction.
Results do not seem correct.	Check the predictions of the model against a case for which an analytical solution is known. Check the values of the parameters.

14.6 Summary Points

- Mathematical models based on the principle of conservation of mass can greatly enhance understanding of the behavior of and lead to principles for design of nanoparticles used for targeting.
- Implementing such models can be performed at the molecular scale, tissue scale, and organism scale, or at combinations of these scales.
- Molecular scale modeling is focused on changes in concentrations of species with respect to time using chemical kinetics.
- Tissue scale modeling adds convection and diffusion within tissues along with reaction terms as in molecular scale modeling.

5. Organism scale modeling uses compartmental modeling with rates of mass exchange between compartments.
6. Once the model is capable of generating accurate predictions of the system's behavior under conditions not yet studied, the equations on which the model is based most likely incorporate the physical phenomena important to the behavior of the nanoparticles.

Acknowledgments

The authors thank our funding sources: NIH (R21 NS051310, K22 DE014386) and Arizona Biomedical Research Commission Grant (#0707).

References

- [1] Lubicher, D., and M. B. G. Manfred, *Modeling Biology Structures, Behaviors, Evolutions*. Cambridge, MA: The MIT Press, 2007, p. 396.
- [2] Caplan, M. R., and E. V. Rosca, "Targeting drugs to combinations of receptors: a modeling analysis of potential specificity," *Ann. Biomed. Eng.*, Vol. 33, No. 8, 2005, pp. 1113–1124.
- [3] West, J. L., and N. J. Halas, "Engineered nanomaterials for biophotonics applications: improving sensing, imaging, and therapeutics," *Ann. Rev. Biomed. Eng.*, Vol. 5, 2003, pp. 285–292.
- [4] Lowery, A., A. M. Gobin, D. S. Emily, J. N. Halas, and J. West, "Immunonanoshells for targeted photothermal ablation of tumor cells," *International Journal of Nanomedicine*, Vol. 1, No. 2, 2006.
- [5] Gao, X., L. Yang, J. A. Petros, F. F. Marshall, J. W. Simons, and S. Nie, "In vivo molecular and cellular imaging with quantum dots," *Curr. Opin. Biotechnol.*, Vol. 16, No. 1, 2005, pp. 63–72.
- [6] Handl, H. L., J. Vagner, H. I. Yamamura, V. J. Hruby, and R. J. Gillies, "Lanthanide-based time-resolved fluorescence of in cyto ligand-receptor interactions," *Anal. Biochem.*, Vol. 330, No. 2, 2004, pp. 242–250.
- [7] Balthasar, S., K. Michaelis, N. Dinauer, H. von Briesen, J. Kreuter, and K. Langer, "Preparation and characterisation of antibody modified gelatin nanoparticles as drug carrier system for uptake in lymphocytes," *Biomaterials*, Vol. 26, No. 15, 2005, pp. 2723–2732.
- [8] Krishnamurthy, V. M., V. Semetey, P. J. Bracher, N. Shen, and G. M. Whitesides, "Dependence of effective molarity on linker length for an intramolecular protein-ligand system," *J. Am. Chem. Soc.*, Vol. 129, No. 5, 2007, pp. 1312–1320.
- [9] Mammen, M., S. Choi, and G. M. Whitesides, "Polyvalent interactions in biological systems: implications for design and use of multivalent ligands and inhibitors," *Angew. Chem. Int. Ed.*, Vol. 37, 1998, pp. 2754–2794.
- [10] Folkman, J., "Tumor angiogenesis: therapeutic implications," *N. Engl. J. Med.*, Vol. 285, No. 21, 1971, pp. 1182–1186.
- [11] Dvorak, H. F., J. A. Nagy, and A. M. Dvorak, "Structure of solid tumors and their vasculature: implications for therapy with monoclonal antibodies," *Cancer Cells*, Vol. 3, No. 3, 1991, pp. 77–85.
- [12] Dreher, M. R., W. Liu, C. R. Michelich, M. W. Dewhirst, F. Yuan, and A. Chilkoti, "Tumor vascular permeability, accumulation, and penetration of macromolecular drug carriers," *J. Natl. Cancer Inst.*, Vol. 98, No. 5, 2006, pp. 335–344.
- [13] Morrison, P. F., M. Y. Chen, R. S. Chadwick, R. R. Lonser, and E. H. Oldfield, "Focal delivery during direct infusion to brain: role of flow rate, catheter diameter, and tissue mechanics," *Am. J. Physiol.*, Vol. 277, No. 4, Pt. 2, 1999, pp. R1218–R1229.
- [14] Jain, R. K., K. D. Janda, and W. M. Saltzman, "Drug discovery and delivery," *Mol. Med. Today*, Vol. 1, No. 1, 1995, p. 4.
- [15] Wang, Y., and F. Yuan, "Delivery of viral vectors to tumor cells: extracellular transport, systemic distribution, and strategies for improvement," *Ann. Biomed. Eng.*, Vol. 34, No. 1, 2006, pp. 114–127.
- [16] Perelson, A. S., and C. DeLisi, "Receptor clustering on a cell surface. I. Theory of receptor cross-linking by ligands bearing two chemically identical functional groups," *Mathematical Biosciences*, Vol. 48, 1980, pp. 71–110.
- [17] Lauffenburger, D. A., and J. J. Linderman, *Receptors Models for Binding, Trafficking and Signaling*, New York, Oxford University Press, 1993, p. 365.

- [18] Shewmake, T., F. Solis, and M. R. Caplan, "Effects of linker properties on multivalent targeting," *Biomacromolecules*, Vol. 9, No. 11, 2008, pp. 3057–3064.
- [19] Morrison, P. F., D. W. Laske, H. Bobo, E. H. Oldfield, and R. L. Dedrick, "High-flow microinfusion: tissue penetration and pharmacodynamics," *Am. J. Physiol.*, Vol. 266, No. 1, Pt. 2, 1994, pp. R292–R305.
- [20] Rosca, E. V., J. M. Stukel, R. J. Gillies, J. Vagner, and M. R. Caplan, "Specificity and mobility of biomacromolecular, multivalent constructs for cellular targeting," *Biomacromolecules*, Vol. 8, No. 12, 2007, pp. 3830–3835.
- [21] Stukel, J. M., J. J. Heys, and M. R. Caplan, "Optimizing delivery of multivalent targeting constructs for detection of secondary tumors," *Ann. Biomed. Eng.*, Vol. 36, No. 7, 2008, pp. 1291–1304.
- [22] Bartlett, D. W., H. Su, I. J. Hildebrandt, W. A. Weber, and M. E. Davis, "Impact of tumor-specific targeting on the biodistribution and efficacy of siRNA nanoparticles measured by multimodality in vivo imaging," *Proc. Natl. Acad. Sci. USA*, Vol. 104, No. 39, 2007, pp. 15549–15554.
- [23] Lemmon, A. R., and E. C. Moriarty, "The importance of proper model assumption in bayesian phylogenetics," *Syst. Biol.*, Vol. 53, No. 2, 2004, pp. 265–277.
- [24] Garfinkel, D., and K.A. Fegley, "Fitting physiological models to data," *Am. J. Physiol.*, Vol. 246, No. 5, Pt. 2, 1984, pp. R641–R650.
- [25] Landaw, E. M., and J. J. DiStefano, 3rd, "Multiexponential, multicompartmental, and noncompartmental modeling. II. Data analysis and statistical considerations," *Am. J. Physiol.*, Vol. 246, No. 5, Pt. 2, 1984, pp. R665–R677.